COMPUTATIONALLY EFFICIENT APPROACH FOR THE MINIMIZATION OF VOLUME CONSTRAINED VECTOR-VALUED GINZBURG-LANDAU ENERGY FUNCTIONAL

R. TAVAKOLI

Abstract. The minimization of volume constrained vector-valued Ginzburg-Landau energy functional is considered in the present study. It has many applications in computational science and engineering, like the conservative phase separation in multiphase systems (such as the spinodal decomposition), phase coarsening in multiphase systems, color image segmentation and optimal space partitioning. A computationally efficient algorithm is presented to solve the space discretized form of the original optimization problem. The algorithm is based on the constrained nonmonotone L^2 gradient flow of Ginzburg-Landau functional followed by a regularization step, which is resulted from the Tikhonov regularization term added to the objective functional, that lifts the solution from the L^2 function space into H^1 space. The regularization step not only improves the convergence rate of the presented algorithm, but also increases its stability bound. The step-size selection based on the Barzilai-Borwein approach is adapted to improve the convergence rate of the introduced algorithm. The success and performance of the presented approach is demonstrated throughout several numerical experiments. To make it possible to reproduce the results presented in this work, the MATLAB implementation of the presented algorithm is provided as the supplementary material.

Keywords. Barzilai-Borwein stepsize; Constrained gradient flow; Ginzburg-Landau functional; Nonmonotine gradient flow; Periodic space tessellation; Spinodal decomposition.

Contents

1. Introduction

In their seminal paper [19], Cahn and Hilliard introduced the following functional to approximate the total Helmholtz free energy of an inhomogeneous system under zero-flux boundary conditions:

$$E(u) = \int_{\Omega} \left(\frac{\varepsilon^2}{2} |\nabla u|^2 + F(u) \right) d\mathbf{x} \tag{1}$$

Date: April 18, 2015.

R. Tavakoli, Department of Materials Science and Engineering, Sharif University of Technology, Tehran, Iran, P.O. Box 11365-9466, tel: 982166165209, fax: 982166005717, email: rtavakoli@sharif.ir.

where E denotes the total free energy of the system, $\Omega \subset \mathbb{R}^d$ $(d = 2, 3)$ is a bounded domain with sufficiently regular boundaries, u denotes the concentration (or phase indicator field), ε is the gradient coefficient which is proportional to the interfacial energy and thickness of the (diffuse) interface between phases, and $F(u)$ denotes the free energy density of a homogeneous system with concentration u. Due to closely related works done by Ginzburg and Landau [37] on the theory of superconductivity in advance of Cahn and Hilliard, functional E is commonly called the Ginzburg-Landau functional in the scientific community. It is however interesting to note that the same form of energy functional has been firstly used by J.D. van der Waals [70] more than 100 years ago to develop the theory of capillarity based on the continuum thermodynamics approach. In [20], Cahn and Hilliard used functional E to study nucleation of second phase in binary solutions using the diffuse interface approach. For this purpose, they computed the Euler-Lagrange equation (with respect to the L^2 inner product) corresponding to functional (1) under the volume constraint on the concentration field. In fact, they looked for the stationary points of the volume constrained Allen-Cahn equation. In [2], the L^2 gradient flow of (1), the Allen-Cahn equation, has been used to study the motion of anti-phase boundaries in crystalline solids:

$$\frac{\partial u}{\partial t} = \varepsilon^2 \Delta u - f(u), \quad (\mathbf{x}, t) \in \Omega \times \mathcal{T}, \quad u(\mathbf{x}, 0) = u_0, \quad \partial_n u|_{\partial\Omega} = 0 \tag{2}$$

where Δ denotes the laplacian operator, $f(u) = F'(u)$, $\mathcal{T} = [0, T]$ denotes the temporal domain, $\partial\Omega$ denotes the boundaries of Ω, $\partial_n u := \nabla u \cdot \mathbf{n}$ and $\mathbf{n}$ denotes the outward unit normal on $\partial\Omega$. The periodic boundary condition is an alternative boundary condition for (2). Because, the Allen-Cahn equation does not essentially conserve the total measure of the concentration field under isolated or periodic boundary conditions, it is called the nonconservative gradient flow of (1) and is commonly used to model the first order phase transition phenomena in materials science, c.f. [66]. To study the spinodal decomposition and coarsening phenomena in binary alloys, the conservative gradient flow of (1), the Cahn-Hilliard equation, has been introduced in [18, 21]:

$$\frac{\partial u}{\partial t} = -\Delta\big(\varepsilon^2 \Delta u - f(u)\big), \quad (\mathbf{x}, t) \in \Omega \times \mathcal{T}, \quad u(\mathbf{x}, 0) = u_0, \quad \partial_n u|_{\partial\Omega} = \partial_n\big(\varepsilon^2 \Delta u - f(u)\big)|_{\partial\Omega} = 0 \tag{3}$$

The Cahn-Hilliard-like equations are commonly used to model second order phase transition phenomena in materials science, c.f. [66]. The original derivation of the Cahn-Hilliard equation was based on the linear irreversible thermodynamics approach in which the variational derivative of (1) has been taken into account as the diffusion potential, c.f. chapter 18 of [4]. Later, it was shown that the Cahn-Hilliard equation is, in fact, the gradient flow of (1) with respect to the H^{-1} inner product, see for instance [32].

Due to their nonlinearity, it is not possible to find analytical solutions of the Allen-Cahn and Cahn-Hilliard equations. Therefore, in practice, using numerical solutions is very common to study the dynamics of these equations. Because the Allen-Cahn and Cahn-Hilliard equations evolve along descent directions of (1), they converge to the stationary points (local minimizers) of (1). The euler explicit time integration approach [66] is the simplest method to solve these equations. Many computational methods have been invented to improve the accuracy, stability and/or efficiency of numerical solution of Allen-Cahn and Cahn-Hilliard equations, for instance: exponential time differencing [25, 46], multigrid [47, 48, 84], adaptive time stepping [26, 39, 85, 88], isogeometric analysis [40, 57], C^1-continuity finite element [87], Sobolev gradient [67–69, 73] and unconditionally energy stable [30, 42, 72, 83] approaches.

As it is mentioned above, the Cahn-Hilliard equation conserves the global measure of u, i.e. $d/dt\ (\int_\Omega u\ d\mathbf{x}) = 0$. Therefore, the steady-state or long-time solutions of the Cahn-Hilliard equation and the Allen-Cahn equation subject to the following volume constraint (in fact, the volume constrained L^2 gradient flow of E) should be identical from the physical point of view:

$$\int_\Omega u(\mathbf{x}, t)\ d\mathbf{x} = \int_\Omega u_0(\mathbf{x})\ d\mathbf{x} \tag{4}$$

However, the minimization path of two approaches, as well as their stationary points will not be essentially identical (consider the nonconvexity of functional E). It is worth to mention that the

numerical solution of Cahn-Hilliard equation involves more challenges than that of the Allen-Cahn equation. This is due to the fact that the Cahn-Hilliard equation is stiffer and its maximum allowable time increment for the stable time integration includes commonly more restriction than that of the Allen-Cahn equation. Therefore, an interesting problem is to compare the behaviors of Cahn-Hilliard and volume constrained Allen-Cahn equations. Regarding to the numerical solution of volume constrained Allen-Cahn equation, there are few works in the literature, to the best of our knowledge. For instance, in [10, 11] the semi-smooth Newton method has been used to solve the volume constrained Allen-Cahn equation. The volume constraint has been managed by the traditional lagrange multiplier approach in these works. By adding a nonlinear nonlocal term to the right hand side of (2), different volume preserving forms of the Allen-Cahn equation have been introduced in [6, 17, 49, 71]. Obviously, the existence of the mentioned nonlocal term increases the complexity and computational cost of the corresponding numerical solution.

Because the field variable u represents the concentration or the volume fraction of the second phase (up to a linear mapping), it should lie in interval $[-1, 1]$ to ensure the physical consistency of the mathematical model. In fact, there are an infinite number of pointwise constraints. The solutions of Allen-Cahn and Cahn-Hilliad equations, however do not essentially satisfy these constraints. A common solution of this problem is to filter u after every time step. However, this treatment is not mathematically rigorous. There were few works in which these constraints have been taken into account during the development of solution algorithms, for instance see [11–13].

The energy functional (1) can be easily extended to model the Helmholtz free energy of multiphase systems. The multiphase version of the Cahn-Hilliard equation, Cahn-Morel equation, has been introduced in [60] by Morel and Cahn to model the spinodal decomposition in ternary systems. Similar to the Cahn-Hilliard equation, the evoluation of concentration fields by the Cahn-Morel equation conserves the total measure of every phase or component under zero-flux or periodic boundary conditions. Later, Cahn-Morel-like equations have been extensively used in literature to study the phase separation, nucleation and coarsening in multiphase systems, for instance see: [7, 14, 22, 24, 27, 29, 44, 45, 50, 54]. Similar to the Allen-Cahn equation, the L^2 gradient flow of multiphase Ginzburg-Landau functional has been extensively used in the literature to model nonconservative multiphase phase transition phenomena, for instance see: [23, 31, 31, 35, 51, 52, 55, 56, 75, 76, 82]. There are few works in which the volume constrained L^2 gradient flow of multiphase Ginzburg-Landau functional has been taken into account. Remarkable works in this regards are [11, 34, 63]. In these works, the pointwise bound and incompressibility constraints are managed by the projection method and the volume constraints are handled by the traditional lagrange multiplier method. For further literature survey on the diffuse interface modeling of multiphase systems, interested readers are referred to: [43, 53, 62, 74].

In the present study, a computationally efficient method is developed to solve the volume constrained L^2 gradient flow of the Ginzburg-Landau functional. The pointwise bound constraints are taken into account in addition to the volume constraint in our method, such that its iterations will be strictly feasible with respect to the set of constraints. The method is constructed based on the projected gradient flow of the free energy functional. Because the projection will be performed with respect to the L^2 norm in the present study, a regularization step is used to control the smoothness of solutions. To this end, the optimization is performed in two steps during each iteration; the projected gradient step followed by the regularization step. The second step of every iteration naturally regularizes the solution while it does not destroy the feasibility of the solution with respect to the set of constraints. Using this approach, we not only regularizes the iterations, but also perform the minimization path on the H^1 space. There were few works in which the minimization of the Ginzburg-Landau functional has been performed on the H^1 space (Sobolev gradient method, c.f. [64]), see for instance [67–69, 73]. However, in contrast to these works, the benefit of our approach is that the bound constraints are consistently taken into account in the solution algorithm. To the best of our knowledge, this is the first effort on the solution of constrained Allen-Cahn equation on H^1 space considering the global volume constraint together with pointwise bound constraints. Similar to [67–69, 73], performing the minimization on the H^1 space makes it possible to use larger time

increments in contrast to the traditional methods. Moreover, due to its intrinsic regularization, its convergence rate to the stationary points of the Ginzburg-Landau functional is faster than that of the L^2 norm based methods. The presented algorithm is then extended to solve the constrained gradient flow of the multiphase Ginzburg-Landau functional. The feasibility of the presented algorithms is supported by computational experiments. It is worth mentioning that the presented algorithms can be extended to solve similar optimization problems. For instance, in [79] the presented algorithm in this study is adapted to solve the multimaterial topology optimization problems (cf. [80]).

2. Minimization of the volume constrained Ginzburg-Landau functional

The minimization problem corresponding to the volume constrained Ginzburg-Landau functional can be written as follows:

$$\min_{u\in\mathcal{D}} \; E(u) \tag{5}$$

where $\mathcal{D}$ denotes the admissible solution domain which is defined as follows:

$$\mathcal{D} := \big\{ v \in \mathcal{U}(\Omega) \;\big|\; \int_\Omega v(\mathbf{x})\; d\mathbf{x} = \Lambda|\Omega|,\; -1 \leqslant v(\mathbf{x}) \leqslant 1 \;\; \texttt{for all } \mathbf{x} \in \Omega \big\}$$

where $\mathcal{U}$ is a sufficiently regular function space, $-1 \leqslant \Lambda \leqslant 1$ and $\Lambda = \big(\int_\Omega u_0(\mathbf{x})\; d\mathbf{x}\big)/|\Omega|$. Since all constraints in $\mathcal{D}$ are linear, $\mathcal{D}$ is convex.

2.1. Preliminaries results on the convex constrained gradient flow.

In this subsection we cover some preliminary known results on the convex constrained optimization that are used to construct our solution algorithms in the present study.

Theorem 2.1. *(orthogonal projection onto a convex set, theorem 12.1.10 of [1]) Let $\mathcal{W}$ be a Hilbert space and $\mathcal{K}$ as a convex closed nonempty subset of $\mathcal{W}$. For all $w \in \mathcal{W}$, there exists a unique $w_\mathcal{K} \in \mathcal{K}$ such that*

$$\|w - w_\mathcal{K}\|^2 = \min_{v\in\mathcal{K}} \|w - v\|^2$$

The orthogonal projection of w onto set $\mathcal{K}$ is shown by operator $\mathscr{P}_\mathcal{K}[w]$ henceforth in this paper, i.e., $w_\mathcal{K} = \mathscr{P}_\mathcal{K}[w]$. Equivalently, $w_\mathcal{K}$ is characterized by the following property:

$$w_\mathcal{K} \in \mathcal{K}, \quad \langle w_\mathcal{K} - w,\; v - w_\mathcal{K}\rangle \geqslant 0, \quad \forall v \in \mathcal{K} \tag{6}$$

where $\langle\cdot,\cdot\rangle$ and $\|\cdot\|$ denote the inner product and associated norm on $\mathcal{W}$, i.e. $\|v\| = \sqrt{\langle v, v\rangle}$.

Proposition 2.2. *Let $\mathcal{W}$ be a Hilbert space and $\mathcal{K}$ as a convex closed nonempty subset of $\mathcal{W}$. Assume that v and w are arbitrary members of $\mathcal{W}$ and their orthogonal projection onto $\mathcal{K}$ are denoted by $v_\mathcal{K}$ and $w_\mathcal{K}$ respectively. Then the following identity holds:*

$$\langle w_\mathcal{K} - v_\mathcal{K},\; w - v\rangle \geqslant \|w_\mathcal{K} - v_\mathcal{K}\|^2 \tag{7}$$

Proof. Replacing v with $v_\mathcal{K}$ in (6) results in:

$$\langle w_\mathcal{K} - w,\; v_\mathcal{K} - w_\mathcal{K}\rangle \geqslant 0 \tag{8}$$

Interchanging v and w in (8) results in:

$$\langle v_\mathcal{K} - v,\; w_\mathcal{K} - v_\mathcal{K}\rangle \geqslant 0 \tag{9}$$

Adding (8) to (9) and expansion of the resulting identity gives:

$$\langle w_\mathcal{K},\; v_\mathcal{K}\rangle - \langle w,\; v_\mathcal{K}\rangle - \|w_\mathcal{K}\|^2 + \langle w,\; w_\mathcal{K}\rangle + \langle v_\mathcal{K},\; w_\mathcal{K}\rangle - \langle v,\; w_\mathcal{K}\rangle - \|v_\mathcal{K}\|^2 + \langle v,\; v_\mathcal{K}\rangle \geqslant 0 \tag{10}$$

Rearrangement of terms in (10) completes the proof. □

Theorem 2.3. *(Euler inequality for convex sets, theorem 10.2.1 of [1]) Let $\mathcal{W}$ be a Hilbert space and $\mathcal{K}$ as a convex closed nonempty subset of $\mathcal{W}$. Assume that functional $J(w) : \mathcal{K} \to \mathbb{R}$ is differentiable at $w \in \mathcal{K}$ with the directional derivative denoted by $J'(w)$. If w^* denotes a local minimum point of $J(w)$ over $\mathcal{K}$, then:*

$$\langle J'(w^*),\; v - w^*\rangle \geqslant 0, \quad \forall v \in \mathcal{K} \tag{11}$$

Proposition 2.4. *(necessary optimality conditions based on the projected gradient) Let $\mathcal{W}$ be a Hilbert space and $\mathcal{K}$ as a convex closed nonempty subset of $\mathcal{W}$. Assume the functional $J(w) : \mathcal{K} \to \mathbb{R}$ is differentiable at $w \in \mathcal{K}$ with the directional derivative denoted by $J'(w)$. If w^* denotes a local minimizer of $J(w)$ over $\mathcal{K}$, then:*

$$J'_{\mathcal{K},\mu}(w^*) = \mathscr{P}_{\mathcal{K}}[w^* - \mu J'] - w^* = 0 \quad \text{a.e.} \tag{12}$$

where $\mu \in \mathbb{R}^+$. Since $\mathscr{P}_{\mathcal{K}}[w - \mu J'] - w$ is equal to the scaled projected gradient of J at w (c.f. [9]), the constrained stationary points of J are roots of the scaled projected gradient with respect to set $\mathcal{K}$. Therefore we call (12) the necessary optimality conditions based on the projected gradient.

Proof. Considering an arbitrary $\mu \in \mathbb{R}^+$, by (11) we have:

$$\langle \mu J'(w^*),\ v - w^* \rangle \geqslant 0, \quad \forall v \in \mathcal{K}$$

Simple algebra results in:

$$\Big\langle w^* - \big(w^* - \mu J'(w^*)\big),\ v - w^* \Big\rangle \geqslant 0, \quad \forall v \in \mathcal{K} \tag{13}$$

Comparing (6) and (13) results in:

$$w^* = \mathscr{P}_{\mathcal{K}}\big[w^* - \mu J'(w^*)\big]$$

almost everywhere, which completes the proof. □

Proposition 2.5. *(descent property of the scaled projected gradient) Let $\mathcal{W}$ be a Hilbert space and $\mathcal{K}$ as a convex closed nonempty subset of $\mathcal{W}$. Assume that functional $J(w) : \mathcal{K} \to \mathbb{R}$ is differentiable at $w \in \mathcal{K}$ with the directional derivative denoted by $J'(w)$. Assume that the scaled projected gradient at $w \in \mathcal{K}$ is denoted by $J'_{\mathcal{K},\mu}(w)$, i.e., $J'_{\mathcal{K},\mu}(w) = \mathscr{P}_{\mathcal{K}}[w - \mu J'(w)] - w$. Then for all $w \in \mathcal{K}$ and $\mu \in \mathbb{R}^+$ we have:*

$$\langle J'(w),\ J'_{\mathcal{K},\mu}(w) \rangle \leqslant -\frac{1}{\mu} \| J'_{\mathcal{K},\mu}(w) \|^2 \tag{14}$$

Proof. Replacing w with $w - \mu J'(w)$ and, then v with w in (7) results in:

$$\langle \mathscr{P}_{\mathcal{K}}[w - \mu J'(w)] - \mathscr{P}_{\mathcal{K}}[w],\ -\mu J'(w) \rangle \geqslant \| \mathscr{P}_{\mathcal{K}}[w - \mu J'(w)] - \mathscr{P}_{\mathcal{K}}[w] \|^2 \tag{15}$$

Since $w \in \mathcal{K}$, $\mathscr{P}_{\mathcal{K}}[w] = w$, therefor,

$$\big\langle \mathscr{P}_{\mathcal{K}}[w - \mu J'(w)] - w,\ J'(w) \big\rangle \leqslant -\frac{1}{\mu} \| \mathscr{P}_{\mathcal{K}}[w - \mu J'(w)] - w \|^2$$

□

Considering proposition 2.5, starting from arbitrary initial guess w^0, functional $J(w)$ can be minimized by the following iterative procedure:

$$w^{n+1} = w^n + \alpha^n J'_{\mathcal{K},\mu^n}(w^n), \qquad n = 0, 1, \dots \tag{16}$$

where $\alpha^n \in (0, 1]$ is chosen according to a suitable globalization strategy. In practice, the scaling factor μ has a significant impact on the convergence rate of (16). Following [9, 78], the scaling factor μ is computed based on the Barzilai and Borwein [5] step size selection approach in the present study. For the sake of convenience, this approach is briefly explained in subsection 2.1.1.

2.1.1. *Computation of gradient scaling factor by the Barzilai-Borwein method.* In [5], a fully explicit approach has been introduced to compute the line search stepsize in the steepest descent method in unconstrained optimization problems. The method was based on the approximation of the Hessian matrix at the n-th step of the optimization by the diagonal matrix $\frac{1}{\mu^n}\mathbf{I}$, where $\mathbf{I}$ denotes the identity matrix and μ^n is computed as follows:

$$\mu^n = \min\{\ \mu^{max},\ \max\{\ \hat{\mu}^n,\ \mu^{min}\}\}, \quad \hat{\mu}^n = \frac{\| s^{n-1} \|^2}{\langle s^{n-1}, y^{n-1} \rangle} \tag{17}$$

where $s^{n-1} = w^n - w^{n-1}$, $y^{n-1} = J'(w^n) - J'(w^{n-1})$, $\mu^{min}, \mu^{max} \in \mathbb{R}$, $0 < \mu^{min} \ll 1 \ll \mu^{max} < \infty$ and $n \geqslant 1$. Later, in [9], the Barzilai-Borwein stepsize selection approach has been adapted to solve

convex constrained optimization problems by computing μ^n in (16) by (17) and computing α^n by GLL nonmonotone line search [41] algorithm. As it has been shown in lemma 2.1 of [78], the Barzilai-Borwein stepsize possesses the spectral property while it uses only the first order information. This property is a key for the success of this approach to economically solve large scale optimization problems, cf. [33] and recent survey [8]. In the present study μ^n is computed based on (17). Following, [78], μ^0 is computed by the following equation:

$$\mu^0 = \frac{1}{\|J_{\mathcal{K},1}(w^0)\|_\infty}, \tag{18}$$

For further details about the Barzilai-Borwein method, interested readers are referred to [5, 8, 9, 33, 78].

2.2. **Constrained gradient flow of the Ginzburg-Landau functional.** Using the descent property of the scaled projected gradient given in the proposition 2.5, the following initial value problem is equivalent to a constrained gradient flow (c.f. [32]) of the Ginzburg-Landau functional,

$$\frac{\partial u}{\partial t} = \mathscr{P}_{\mathcal{D}}[u - \mu E'(u)] - u, \quad u(\mathbf{x}, 0) = u_0(\mathbf{x}) \tag{19}$$

where $\mu \in \mathbf{R}^+$ and $E'(u)$ denotes the directional derivative of E at u. It is easy to show that, by starting from an initial guess $u_0 \in \mathcal{D}$, $E(u)$ decreases as u evolves based on equation (19), while u lies on the admissible set $\mathcal{D}$. The later claim is evident due to the existence of projection operator at right hand side of (19). The former claim can be proved as follows:

$$\frac{\partial E(u)}{\partial t} = \big\langle E'(u),\ \frac{\partial u}{\partial t} \big\rangle \overset{(19)}{=} \big\langle E'(u),\ \mathscr{P}_{\mathcal{D}}[u - \mu E'(u)] - u \big\rangle \overset{(14)}{\leqslant} -\frac{1}{\mu}\ \|\mathscr{P}_{\mathcal{D}}[u - \mu E'(u)] - u\|^2$$

Therefore, $E(u(\mathbf{x}, t)) \leqslant E(u_0(\mathbf{x}))$ for all $t \geqslant 0$. Assume we have the homogeneous Neumann, zero-flux, boundary conditions for u on boundaries of Ω. Computing the directional derivative of E with respect to L^2 norm and its substitution into (19) leads to the following parabolic PDE:

$$\left\{ \begin{array}{rcll} \frac{\partial u}{\partial t} & = & \mathscr{P}_{\mathcal{D}}\big[u + \mu\big(\varepsilon^2 \Delta u - f(u)\big)\big] - u & \texttt{in} \quad \Omega \times \mathcal{T} \\ u & = & u_0(\mathbf{x}) & \texttt{in} \quad \Omega \times \{t = 0\} \\ \partial_n u & = & 0 & \texttt{on} \quad \partial\Omega \times \mathcal{T} \end{array} \right. \tag{20}$$

Because the directional derivative of E is computed with respect to the L^2 norm, the Hilbert space $\mathcal{W}$ used in the previous subsection should be replaced by the function space $L^2(\Omega)$ here, i.e. for every $w \in L^2(\Omega)$ we have:

$$\mathscr{P}_{\mathcal{D}}[w] = \min_{v \in \mathcal{D}} \|w - v\|^2_{L^2(\Omega)} \tag{21}$$

It implies that $\mathscr{P}_{\mathcal{D}}[w] \in L^2(\Omega)$. Therefore, the regularity of solution of (20) is not essentially better than $L^2(\Omega)$. According to our numerical experiments, solutions of (20) are not always sufficiently smooth. Consequently, undesired behaviors, that decrease the rate of convergence to the stationary point of $E(u)$, are observed in some cases (c.f. numerical results section in the present study). To cope this loss of regularity, a heuristic approach is employed in the present study. It is based on the Tikhonov regularization of the original optimization problem by the addition of H^1-seminorm of u to $E(u)$, as follows:

$$\tilde{E}(u) = E(u) + E_\varrho(u), \quad E_\varrho(u) := \frac{\varrho}{2} \int_\Omega |\nabla u|^2 \ d\mathbf{x} \tag{22}$$

where $\varrho \in \mathbb{R}^+$ is the regularization parameter that controls the smoothness of solution. Then, we minimize the regularized counterpart of $E(u)$, i.e. $\tilde{E}(u)$ instead of $E(u)$. For this purpose, every iteration of the optimization is decomposed into two sequential steps. At the first step $E(u)$ is minimized by solving the time discretized form of (20) with sufficiently small time increment $\Delta t \leqslant 1$ to find $v(\mathbf{x})$. Then, E_ϱ is minimized by solving the time discretized form of the following parabolic PDE with the time stepsize Δt, homogeneous Neumann boundary condition and $v(\mathbf{x})$ as the initial condition:

$$\frac{\partial u}{\partial t} = \varrho\ \Delta u, \quad u(\mathbf{x}, t_0) = v(\mathbf{x}) \tag{23}$$

Assume that the temporal domain is discretized into a uniform grid with the time stepsize Δt. Moreover, assume that the superscript n denotes the field variables at time level n, i.e. $u^n := u(\mathbf{x}, t = n\Delta t)$. The numerical algorithm developed in the present study is independent of the method used for the spatial domain discretization. However, for the sake of convenience, we assume that the spatial domain is discretized into a uniform Cartesian grid with grid size Δx in all directions. Moreover, it is assumed that the spatial derivatives are computed by the second order central finite difference scheme. Although we present our algorithm for the case of homogeneous Neumann boundary conditions, it is also valid for the case of periodic boundary conditions. The solution algorithm to solve (5) in the present study can be expressed as follows:

Algorithm 1. Two-step constrained gradient flow of Ginzburg-Landau functional

Step 0. Initialization: given Ω, u_0, ε, $F(u)$, ϱ, μ^{min}, μ^{max}, $\Delta t \in (0, 1]$, parameters related to the spatial discretization and stopping criteria parameters n^{max} and $\delta > 0$. If $u_0 \notin \mathcal{D}$ then $u_0 = \mathscr{P}_{\mathcal{D}}[u_0]$, set $n \to 0$ and $u^n = u_0$. Compute μ^0 by the following equation:

$$\mu^0 = 1/\|\mathscr{P}_{\mathcal{D}}\big(u^0 + \varepsilon^2 \Delta u^0 - f(u^0)\big) - u^0\|_\infty \tag{24}$$

Step 1. Iterations

1.1 Given u^n, if $n \geqslant 1$ compute μ^n according to the following equations:

$$\hat{\mu}^n = \frac{\|u^n - u^{n-1}\|^2}{\big\langle u^n - u^{n-1}, \varepsilon^2 \Delta(u^{n-1} - u^n) + f(u^n) - f(u^{n-1})\big\rangle} \tag{25}$$

$$\mu^n = \min\{\ \mu^{max},\ \max\{\ \hat{\mu}^n,\ \mu^{min}\}\}, \tag{26}$$

1.2 Given u^n, compute v^n by solving (20) with the zero-flux boundary condition for one time-step by the Euler explicit time integration method, as follows:

$$v^n = u^n + \Delta t\Big[\mathscr{P}_{\mathcal{D}}\big[u^n + \mu^n\big(\varepsilon^2 \Delta u^n - f(u^n)\big)\big] - u^n\Big] \tag{27}$$

1.3 Given v^n, compute u^{n+1} by solving (23) with the zero-flux boundary condition for one time step by the Euler implicit tim integration method, as follows:

$$u^{n+1} = v^n + \Delta t\ \varrho\ \Delta u^{n+1} \tag{28}$$

Step 2. Stopping criteria: If $n = n^{max}$ or $\|u^{n+1} - u^n\|_{L^2(\Omega)} \leqslant \delta$ stop the iterations, else set $n \to n + 1$ and goto step 1.

Remark 2.6. To ensure the global convergence of algorithm 1, it is essential to determine the time stepsize Δt according to a globalization strategy, for instance the GLL nonmonotone line search approach [41]. In the present study, we simply take Δt as a sufficiently small and constat value such that the algorithm behaves almost monotonically. According to our numerical experiments, the value of $\Delta t \approx 0.5$ is a reasonable choice to balance between the performance and monotonicity of algorithm 1.

Rearranging terms in (28) results in the following Helmholtz equation under the homogeneous Neumann boundary conditions:

$$(I - \zeta\Delta)\ u^{n+1} = v^n \tag{29}$$

where I denotes the identity operator and $\zeta = \Delta t\ \varrho$. Considering remark 2.6, the time stepsize is fixed during our computations in the present study. As a result, the Helmholtz operator $(I - \zeta\Delta)$ is fixed during our computations. Therefore, it is economical to decompose the discretized form of this operator by the incomplete Cholesky factorization once and reuse it in the course of computations.

In fact, step 1.3 of algorithm 1 lifts the solution from $L^2(\Omega)$ to $H^1(\Omega)$, as it is illustrated in the following proposition:

Proposition 2.7. *When $\zeta > 0$, step 1.3, the regularization step, of algorithm 1 is equivalent to the transition of temporary solution v^n from $L^2(\Omega)$ to $H^1(\Omega)$, where the function space $H^1(\Omega)$ is occupied with the following inner product: $(f,g)_{H^1(\Omega)} := \int_\Omega (fg + \zeta \nabla f \cdot \nabla g)\ d\mathbf{x}$ for every $f, g \in H^1(\Omega)$.*

Proof. Because the projected gradient is computed with respect to the L^2 inner product, $v^n \in L^2(\Omega)$. Taking the inner product of both sides of (29) with an arbitrary function $w \in H^1(\Omega)$ results in:

$$\int_\Omega (u^{n+1} - \zeta \Delta\ u^{n+1})\ w\ d\mathbf{x} = \int_\Omega\ v^n\ w\ d\mathbf{x}$$

applying the divergence theorem and using the homogeneous Neumann boundary conditions result in:

$$\int_\Omega (u^{n+1}\ w - \zeta\ \nabla u^{n+1} \cdot \nabla w)\ d\mathbf{x} = \int_\Omega\ v^n\ w\ d\mathbf{x}$$

i.e. $(u^{n+1},\ w)_{H^1(\Omega)} = (v^n,\ w)_{L^2(\Omega)}$. Therefore, the proof is directly followed by the Riesz representation theorem (cf. [1]). □

It is easy to show that under mild conditions, the iterations generated by algorithm 1 are strictly feasible with respect to the constraints set $\mathcal{D}$. This property is proved in the following proposition.

Proposition 2.8. *If $u_0 \in L^2(\Omega)$ and $\Delta t \in (0, 1]$ in algorithm 1, then $u^{n+1} \in \mathcal{D}$ for $n = 0, 1, \dots$.*

Proof. We first show that solutions of (27) lie in $\mathcal{D}$. Rearrangement of terms in (27) results in:

$$v^n = (1 - \Delta t)\ u^n + \Delta t\ w^n \tag{30}$$

where $w^n := \mathscr{P}_{\mathcal{D}}\big[u^n + \mu\big(\varepsilon^2 \Delta u^n - f(u^n)\big)\big]$. Because $u^n, w^n \in \mathcal{D}$, $0 < \Delta t \leqslant 1$ and $\mathcal{D}$ is convex, (30) ensures that $v^n \in \mathcal{D}$. Now, we show that if $v^n \in \mathcal{D}$, solutions of (28) lie in $\mathcal{D}$. It is well known that under the homogeneous Neumann boundary conditions, the linear heat equation in the continuous form, i.e. (23), as well as the presented discretized form, i.e. (28), satisfies the maximum principles. Therefore, if v^n satisfies the pointwise bound constraints then u^{n+1} will satisfies the pointwise bound constraints too. The spatial integration of both sides of (28) results in:

$$\int_\Omega u^{n+1}\ d\mathbf{x} = \int_\Omega v^n\ d\mathbf{x} + \zeta\ \int_\Omega \Delta u^{n+1}\ d\mathbf{x}$$

By applying the divergence theorem we have:

$$\int_\Omega u^{n+1}\ d\mathbf{x} = \int_\Omega v^n\ d\mathbf{x} + \zeta\ \int_{\partial\Omega} \nabla u^{n+1} \cdot \mathbf{n}\ d\mathbf{x} \tag{31}$$

Because $v^n \in \mathcal{D}$ the first term in the right hand side of (31) is equal to $\Lambda|\Omega|$. the second term in the right hand side of (31) vanishes by applying the homogeneous Neumann boundary conditions. Therefore, u^{n+1} satisfies the volume constraint. □

It is worth to mention that algorithm 1 has some similarities to the Sobolev gradient flow method [67–69, 73], in which resulted solutions have the H^1 regularity. However, the essential difference of algorithm 1 and the Sobolev gradient flow method is that the second step of algorithm 1 acts on the temporal solution to improve its regularity while in the Sobolev gradient flow method, the directional derivative of the energy functional is computed with respect to the H^1 inner product, and then the gradient flow is exploited with the corresponding H^1 gradient.

Having an efficient algorithm to solve the projection problem (21) is a key for the efficiency of algorithm 1. Due to the existence of pointwise bound constraints in $\mathcal{D}$, there is not an explicit linear operator that projects a trial point onto $\mathcal{D}$. However, in the following subsection, it is shown that (21) can be solved efficiently by an iterative algorithm up to the machine precision accuracy.

2.3. **Orthogonal projection onto $\mathcal{D}$.** The projection of trial point $w \in L^2(\Omega)$ onto $\mathcal{D}$, problem (21), can be re-stated as follows:

$$\min_{v\in\mathcal{B}} \frac{1}{2}\ \|v-w\|^2_{L^2(\Omega)} \quad \texttt{subject to}: \quad \int_\Omega v(\mathbf{x})\ d\mathbf{x} = \Lambda|\Omega| \tag{32}$$

where box $\mathcal{B}$ is defined as follows: $\mathcal{B} := \big\{v \in \mathcal{U}(\Omega)\ \big|\ -1 \leqslant v(\mathbf{x}) \leqslant 1 \ \ \texttt{for all } \mathbf{x} \in \Omega\big\}$. Obviously the optimization problem (32) is convex and has a unique solution. The unique solution of (32) is equal to the unique constrained ($w \in \mathcal{B}$) stationary point of the following augmented lagrangian:

$$\mathcal{L}(v,\lambda) = \frac{1}{2}\ \|v-w\|^2_{L^2(\Omega)} + \lambda\ \left(\int_\Omega v(\mathbf{x})\ d\mathbf{x} - \Lambda|\Omega|\right)$$

where λ is the lagrange multiplier corresponding to the volume constraint. Assume λ^* denotes the value of λ at the stationary point of the constrained lagrangian $\mathcal{L}$. Then, by taking the first variation of $\mathcal{L}$ with respect to v and using the necessary optimality conditions based on the projected gradient approach (c.f. proposition 2.4), the optimal solution of (32), denoted by v^*, can be computed by the following equation:

$$v^* = \mathscr{P}_{\mathcal{B}}[w-\lambda^*] \quad \texttt{a.e. in}\ \ \Omega$$

It is well-know that the projection onto box $\mathcal{B}$ is a convex separable optimization problem with the following explicit solution (cf. chapter 10 of [1]):

$$\mathscr{P}_{\mathcal{B}}[v] = \max(-1,\ \min(1,\ v))$$

therefore,

$$v^* = v(\lambda^*), \quad \texttt{where} \quad v(\lambda) = \max(-1,\ \min(1,\ w(\mathbf{x}) - \lambda)) \tag{33}$$

Finally λ^* is computed by the substitution of v^* into the volume constraint and finding the unique root of function $g(\lambda)$, which is defined as follows:

$$g(\lambda^*) = 0, \quad \texttt{where} \quad g(\lambda) := \int_\Omega v(\lambda)\ d\mathbf{x} - \Lambda|\Omega|$$

The remaining part of solving (32) is introducing an efficient algorithm to find the root of $g(\lambda)$.

Proposition 2.9. *$g(\lambda)$ is a continuous piecewise linear and monotonically non-increasing function of λ.*

Proof. Define functions $\lambda^L, \lambda^U \in \mathcal{U}(\Omega)$ as follows:

$$\lambda^L = w + 1, \quad \lambda^U = w - 1,$$

It is clear that $\lambda^U \leqslant \lambda^L$. Considering (33) we have:

$$v(\lambda) = \begin{cases} 1, & \texttt{if} \quad \lambda \leqslant \lambda^U, \\ w-\lambda, & \texttt{if} \quad \lambda^U \leqslant \lambda \leqslant \lambda^L, \\ -1, & \texttt{if} \quad \lambda \geqslant \lambda^L. \end{cases} \tag{34}$$

Considering (34), $v(\lambda)$ is a continuous piecewise linear and monotonically non-increasing function of λ. Since we have $g(\lambda) = \int_\Omega v(\lambda)\ d\Omega - \Lambda|\Omega|$, $g(\lambda)$ is also a continuous piecewise linear and monotonically non-increasing function of λ. □

Corollary 2.10. *Let $\lambda_{min} = \min(\lambda^U)$ and $\lambda_{max} = \max(\lambda^L)$, then three situations are possible: 1) $\lambda^* = \lambda_{min}$, 2) $\lambda^* = \lambda_{max}$, 3) $\lambda^* \in (\lambda_{min}, \lambda_{max})$ and $g(\lambda_{min})\ g(\lambda_{max}) < 0$.*

Proof. Because, (32) has a unique solution, the root of $g(\lambda)$ is unique. Considering (34), the maximum value of g happens at $\lambda = \lambda_{min}$. Considering (34), $v(\lambda_{min}) = 1$. Therefore $g(\lambda_{min}) = |\Omega|(1-\Lambda) \geqslant 0$. Similarly, the least value of g happens at $\lambda = \lambda_{max}$ and $g(\lambda_{max}) = -|\Omega|(1+\Lambda) \leqslant 0$. Thus, either of situations mentioned in the statement of the corollary happens in practice. □

Therefore, the unique root of $g(\lambda)$ can be efficiently computed by starting from the searching interval $[\lambda_{min}, \lambda_{max}]$ and using the bisection root finding algorithm. Considering the limited precision of digital computers, in practice, the root of g can be computed up to the machine precision in a finite number of bisection steps. According to our numerical experiments, the cost of this root finding procedure is negligible in contrast to the overall computational cost of algorithm 1.

3. Minimization of the mass constrained vector-valued Ginzburg-Landau functional

The two-step constrained gradient flow approach introduced in section 2 will be extended to multiphase systems in this section. The minimization problem corresponding to the volume constrained multiphase Ginzburg-Landau functional, the multiphase analog of (5), can be written as follows:

$$\min_{\mathbf{u}\in\mathcal{A}} \mathbf{E}(\mathbf{u}) := \sum_{i=1}^{p} \int_{\Omega} \frac{\varepsilon^2}{2} |\nabla u_i|^2 \, d\mathbf{x} + \int_{\Omega} \mathbf{F}(\mathbf{u}) \, d\mathbf{x} \tag{35}$$

where $p \geqslant 2$ denotes the number of phases, u_i denotes the concentration field corresponding to i-th phase, $\mathbf{u} := \{u_1, \ldots, u_p\}$ denotes the vector valued concentration field, $\mathbf{F}(\mathbf{u}(\mathbf{x}))$ denotes the free energy density of a homogeneous system with concentration $\mathbf{u} = \mathbf{u}(\mathbf{x})$ and $\mathcal{A}$ denotes the admissible solution domain formed by the set of constraints. There are three kinds of constraints in $\mathcal{A}$ which are described below. Similar to the two-phase case, there are pointwise bound constraints on fields variables u_i, i.e.:

$$-1 \leqslant u_i \leqslant 1, \quad i = 1, \ldots, p \tag{36}$$

There are p volume constraints on the total measure of each phase inside Ω:

$$\int_{\Omega} u_i \, d\mathbf{x} = \Lambda_i |\Omega|, \quad i = 1, \ldots, p \tag{37}$$

where Λ_i $(i = 1, \ldots, p)$ is proportional to the volume (mass) fraction of i-th phase in Ω. Obviously $-1 \leqslant \Lambda_i \leqslant 1$ and $\sum_{i=1}^{p} \Lambda_i = 2 - p$. Assuming the initial concentration field, denoted by $\mathbf{u_0} = \{u_{1,0}, \ldots, u_{p,0}\}$ satisfies (37) then we have: $\Lambda_i = \big(\int_{\Omega} u_{i,0}(\mathbf{x}) \, d\mathbf{x}\big)/|\Omega|$ for $i = 1, \ldots, p$. Unlike the two-phase case, there are additional pointwise constraints due to the incompressibility of phases, i.e. the sum of concentration fields at every point $\mathbf{x} \in \Omega$ should be equal to a constant value, unity up to a linear mapping, i.e.:

$$\sum_{i=1}^{p} u_i = 2 - p \tag{38}$$

It is worth mentioning that, the intersection of (36) and (38) is commonly called the Gibbs p-simplex in the materials science literature, due to the seminal work of Willard Gibbs [36] to study the thermodynamics of inhomogeneous systems. Therefore, the admissible set $\mathcal{A}$ can be expressed as follows:

$$\mathcal{A} := \left\{ \mathbf{v} \in \mathcal{U}^p(\Omega) \;\middle|\; \begin{array}{ll} \sum_{i=1}^{p} v_i = 2 - p, & \\ \int_{\Omega} v_i \, d\mathbf{x} = \Lambda_i |\Omega|, & i = 1, \ldots, p \\ -1 \leqslant v_i \leqslant 1, & i = 1, \ldots, p \end{array} \right\}$$

where $\mathbf{v} = \{v_1, \ldots, v_p\}$. The constraint qualification is a common requirement for the success of optimization algorithms from both the theoretical and practical points of view (cf. [65]). To obtain the qualification of constraints for linearly constrained optimization problems, it is sufficient to show that the equality constraints are linearly independent and that there exists a feasible point satisfying all inequalities strictly. However, the equality constraints in $\mathcal{A}$ are not linearly independent. Assuming that $\mathcal{A}$ is nonempty, to ensure the constraint qualification, we can remove u_p from the set of unknown vectors using equality constraints (38) $(u_p = 2 - p - \sum_{i=1}^{p-1} u_i)$. Therefore, we redefine the admissible set $\mathcal{A}$ in the present study as follows:

$$\mathcal{A} \overset{\texttt{redefine}}{:=} \left\{ \mathbf{v} \in \mathcal{U}^{p-1}(\Omega) \;\middle|\; \begin{array}{ll} \int_{\Omega} v_i \, d\mathbf{x} = \Lambda_i |\Omega|, & i = 1, \ldots, p-1 \\ -1 \leqslant v_i \leqslant 1, & i = 1, \ldots, p-1 \\ 1 - p \leqslant \sum_{i=1}^{p-1} v_i \leqslant 3 - p, & \end{array} \right\}$$

where $\mathbf{v}$ is redefined as $\mathbf{v} = \{v_1, \ldots, v_{p-1}\}$. Therefore, it is sufficient to compute u_i for $i = 1, \ldots, p-1$, and then to compute u_p by: $u_p = 2 - p - \sum_{i=1}^{p-1} u_i$. For the purpose of convenience, henceforth, both of $\{u_1, \ldots, u_p\} \in \mathcal{U}^p$ and $\{u_1, \ldots, u_{p-1}\} \in \mathcal{U}^{p-1}$ will be denoted by the vector field $\mathbf{u}$. Since all constraints in $\mathcal{A}$ are linear, $\mathcal{A}$ is convex. Therefore (35) is a convex constrained minimization problem.

Similar to section 2.2 we substitute the function space $\mathcal{U}$ in the definition of $\mathcal{A}$ by $L^2(\Omega)$. Using the theory of convex constrained gradient flow developed in section 2.1, similar to section 2.2, the constrained gradient flow of the vector-valued Ginzburg-Landau functional results in the following initial value problem:

$$\frac{\partial \mathbf{u}}{\partial t} = \mathscr{P}_{\mathcal{A}}[\mathbf{u} - \mu \mathbf{E}'(\mathbf{u})] - \mathbf{u}, \quad \mathbf{u}(\mathbf{x}, 0) = \mathbf{u_0}(\mathbf{x}) \tag{39}$$

where $\mathbf{u} = \{u_1, \ldots, u_{p-1}\}$, $\mathscr{P}_{\mathcal{A}}$ denotes the orthogonal projection operator from $\big(L^2(\Omega)\big)^{p-1}$ onto $\mathcal{A}$, $\mu \in \mathbf{R}^+$, $\mathbf{u_0} \in \mathcal{A}$ and $\mathbf{E}'(\mathbf{u}) \in \big(L^2(\Omega)\big)^{p-1}$ denotes the directional derivative of $\mathbf{E}$ at $\mathbf{u}$. Considering the homogeneous Neumann boundary conditions on $\partial\Omega$ and constraint $u_p = 2 - p - \sum_{i=1}^{p-1} u_i$, straightforward derivation results in: $\mathbf{E}'(\mathbf{u}) = \big\{E_1'(\mathbf{u}), \ldots, E_{p-1}'(\mathbf{u})\big\}$, where

$$E_i'(\mathbf{u}) = \big(f_i(\mathbf{u}) - \varepsilon^2 \Delta u_i\big) - \big(f_p(\mathbf{u}) - \varepsilon^2 \Delta u_p\big), \quad i = 1, \ldots, p-1 \tag{40}$$

where $f_i(\mathbf{u})$ denotes the partial derivative of $\mathbf{F}(\mathbf{u})$ with respect to u_i, i.e. $f_i(\mathbf{u}) = \partial \mathbf{F}(\mathbf{u})/\partial u_i$.

Similar to (22), the optimization problem (35) can be regularized by the addition of H^1-seminorm of $\mathbf{u}$ to $\mathbf{E}(\mathbf{u})$, as follows:

$$\tilde{\mathbf{E}}(\mathbf{u}) = \mathbf{E}(\mathbf{u}) + \mathbf{E}_\varrho(\mathbf{u}), \quad \mathbf{E}_\varrho(\mathbf{u}) := \frac{\varrho}{2} \sum_{i=1}^{p} \int_\Omega |\nabla u_i|^2 \, d\mathbf{x} \tag{41}$$

where $\varrho \in \mathbb{R}^+$ is the regularization parameter that controls the smoothness of solution. Similar to approach discussed in section 2.2, the minimization of regularized functional $\tilde{\mathbf{E}}(\mathbf{u})$ will be done by the presented two steps approach. Similar to (23), in the second step of optimization, the following parabolic system of PDEs should be solved under the homogeneous Neumann boundary conditions:

$$\frac{\partial \mathbf{u}}{\partial t} = \varrho \, \mathbf{\Delta u}, \quad \mathbf{u}(\mathbf{x}, t_0) = \mathbf{v}(\mathbf{x}) \tag{42}$$

where $\mathbf{u} = \big\{u_1, \ldots, u_{p-1}\big\}$, $\mathbf{\Delta}$ denotes the vector-valued classical laplacian operator, i.e. $\mathbf{\Delta u} = \{\Delta u_1, \ldots, \Delta u_{p-1}\}$ and $\mathbf{v} = \big\{v_1, \ldots, v_{p-1}\big\}$ denotes the minimizer of the optimization problem (35).

Assume that the temporal domain is discretized into a uniform grid with the time stepsize Δt. Moreover, assume that the superscript n denotes the field variable at time level n, i.e. $\mathbf{u}^n := \mathbf{u}(\mathbf{x}, t = n\Delta t)$. Similar to section 2.2, our solution algorithm to solve (5) can be expressed as follows:

Algorithm 2. Two-step constrained gradient flow of vector-valued GL functional

Step 0. Initialization: given Ω, $\mathbf{u_0}$, ε, $\mathbf{F}(\mathbf{u})$, ϱ, μ^{min}, μ^{max}, $\Delta t \in (0,1]$, parameters related to the spatial discretization and stopping criteria parameters n^{max} and $\delta > 0$. If $\mathbf{u_0} \notin \mathcal{A}$ then $\mathbf{u_0} = \mathscr{P}_{\mathcal{A}}[\mathbf{u_0}]$, set $n \to 0$ and $\mathbf{u}^n = \mathbf{u_0}$. Compute μ^0 by the following equation:

$$\mu^0 = 1/\|\mathscr{P}_{\mathcal{A}}\big[\mathbf{u}^0 - \mathbf{E}'(\mathbf{u}^0)\big] - \mathbf{u}^0\|_\infty \tag{43}$$

Step 1. Iterations

1.1 Given $\mathbf{u}^n = \{u_1^n, \ldots, u_{p-1}^n\}$, if $n \geqslant 1$ compute μ^n by the following equation:

$$\mu^n = \min\{\ \mu^{max},\ \max\{\ \hat{\mu}^n,\ \mu^{min}\}\}, \quad \hat{\mu}^n = \frac{\|\mathbf{u}^n - \mathbf{u}^{n-1}\|^2}{\big\langle \mathbf{u}^n - \mathbf{u}^{n-1},\ \mathbf{E}'(\mathbf{u}^n) - \mathbf{E}'(\mathbf{u}^{n-1})\big\rangle} \tag{44}$$

1.2 Given $\mathbf{u}^n = \{u_1^n, \ldots, u_{p-1}^n\}$, compute $\mathbf{v}^n = \{v_1^n, \ldots, v_{p-1}^n\}$ by solving (39) under the zero-flux boundary conditions for one time-step with the Euler explicit time integration, as follows:

$$\mathbf{v}^n = \mathbf{u}^n + \Delta t\Big[\mathscr{P}_{\mathcal{A}}\big[\mathbf{u}^n - \mu\ \mathbf{E}'(\mathbf{u}^n)\big] - \mathbf{u}^n\Big] \tag{45}$$

1.3 Given $\mathbf{v}^n = \{v_1^n, \ldots, v_{p-1}^n\}$, compute $\mathbf{u}^{n+1} = \{u_1^{n+1}, \ldots, u_{p-1}^{n+1}\}$ by solving (42) with the zero-flux boundary conditions for one time step by the Euler implicit tim integration, as follows:

$$\mathbf{u}^{n+1} = \mathbf{v}^n + \Delta t\ \varrho\ \boldsymbol{\Delta}\mathbf{u}^{n+1} \tag{46}$$

1.4 Compute u_p^{n+1} by $u_p^{n+1} = 2 - p - \sum_{i=1}^{p-1} u_i^{n+1}$.

Step 2. Stopping criteria: If $n = n^{max}$ or $\sum_{i=1}^{p-1} \|u_i^{n+1} - u_i^n\|_{L^2(\Omega)} \leqslant \delta$ stop the iterations, else set $n \to n+1$ and goto step 1.

Note that algorithm 2 directly inherits properties of algorithm 1 mentioned in section 2.2. They are briefly mentioned below.

Proposition 3.1. *When $\varrho > 0$, step 1.3 and 1.4 of algorithm 2 lift the temporary solution $\mathbf{v}^n$ from $\big(L^2(\Omega)\big)^{p-1}$ to $\big(H^1(\Omega)\big)^p$.*

Proof. The proof is identical to the proof of proposition 2.7. □

Proposition 3.2. *If $\mathbf{u_0} \in \big(L^2(\Omega)\big)^p$ and $\Delta t \in (0,1]$ in algorithm 2 then $\mathbf{u}^{n+1} \in \mathcal{A}$ for $n = 0, 1, \ldots$.*

Proof. The proof is identical to the proof of proposition 2.8. The only remained job here is to show that $\mathbf{u}^{n+1}$ respects constraint $1 - p \leqslant \sum_{i=1}^{p-1} u_i^{n+1} \leqslant 3 - p$ or equivalently $-1 \leqslant u_p^{n+1} \leqslant 1$. Equation (46) in algorithm 2 can be rewritten as follows:

$$u_i^{n+1} = v_i^n + \zeta \Delta u_i^{n+1}, \quad i = 1, \ldots . p-1 \tag{47}$$

where $\zeta = \Delta t\ \varrho$. Summing over $p-1$ equations in (47) and using identity $u_p = 2 - p - \sum_{i=1}^{p-1} u_i$ results in:

$$u_p^{n+1} = u_p^n + \zeta \Delta u_p^{n+1} \tag{48}$$

Considering $-1 \leqslant u_p^n \leqslant 1$ and the properties of laplacian operator results in $-1 \leqslant u_p^{n+1} \leqslant 1$. □

In the following subsection an efficient algorithm is presented for the projection of trial points onto $\mathbf{A}$.

3.1. **Orthogonal projection onto $\mathcal{A}$.** The projection of trial point $\mathbf{w} \in \left(L^2(\Omega)\right)^{p-1}$ onto $\mathcal{A}$ can be expressed as follows:

$$\min_{\mathbf{v}\in\mathcal{A}} \frac{1}{2} \|\mathbf{v}-\mathbf{w}\|^2_{(L^2(\Omega))^{p-1}} \tag{49}$$

Assuming $\mathcal{A} \neq \emptyset$, because the objective functional is strictly convex and all constraints are linear in in (49), it has a unique solution (cf. [1]). After the spatial discretization, (49) will be a quadratic programming (QP) problem. There are many numerical methods to solve a general QP problem (cf. [16, 61, 86]). However, their computational cost and memory usage increase rapidly with the problem size (the problem size here denotes the dimension of infinite dimensional vector $\mathbf{w}$ field after the space discretization). In [77], three efficient algorithms have been developed by the current author to solve problems with structures similar to (49). According to the numerical results presented in [77], the computational cost and memory usage of these algorithms scale linearly with the problem size. Algorithm #1 of [77] will be adapted here to solve (49).

Lets to define the following sets:

$$\mathcal{A}_1 := \left\{\mathbf{v}=\{v_1,\ldots,v_{p-1}\} \in \left(L^2(\Omega)\right)^{p-1} \;\middle|\; 1-p \leqslant \sum_{i=1}^{p-1} v_i \leqslant 3-p\right\}$$

$$\mathcal{A}_2 := \left\{\mathbf{v}=\{v_1,\ldots,v_{p-1}\} \in \left(L^2(\Omega)\right)^{p-1} \;\middle|\; \int_\Omega v_i \, d\mathbf{x} = \Lambda_i|\Omega|, \quad i=1,\ldots,p-1\right\}$$

$$\mathcal{A}_3 := \left\{\mathbf{v}=\{v_1,\ldots,v_{p-1}\} \in \left(L^2(\Omega)\right)^{p-1} \;\middle|\; -1 \leqslant v_i \leqslant 1, \quad i=1,\ldots,p-1\right\}$$

Obviously, $\mathbf{A} = \mathbf{A}_1 \cap \mathbf{A}_2 \cap \mathbf{A}_3$. By straightforward derivation, it is easy to shown that the optimization problem corresponding to the projection onto $\mathbf{A}_1$, $\mathbf{A}_2$ and $\mathbf{A}_3$ are convex separable problems with the following explicit solutions (cf. chapter 10 of [1] and chapter 8 of [16]):

$$\mathscr{P}_{\mathcal{A}_1}[\mathbf{v}] = \{w_1,\ldots,w_{p-1}\}, \quad w_i = v_i - \frac{\min\left(s(\mathbf{v})+p-1,\ 0\right)}{p-1} - \frac{\max\left(s(\mathbf{v})+p-3,\ 0\right)}{p-1}, \ \ i=1,\ldots,p-1$$

$$\mathscr{P}_{\mathcal{A}_2}[\mathbf{v}] = \{w_1,\ldots,w_{p-1}\}, \quad w_i = v_i + \Lambda_i - \frac{1}{|\Omega|}\int_\Omega v_i \, d\mathbf{x}, \ \ i=1,\ldots,p-1$$

$$\mathscr{P}_{\mathcal{A}_3}[\mathbf{v}] = \{w_1,\ldots,w_{p-1}\}, \quad w_i = \max(-1,\ \min(v_i,\ 1)), \ \ i=1,\ldots,p-1$$

where $s(\mathbf{v}) = \sum_{j=1}^{p-1} v_j$. Using above indentities and alternating projection algorithm (cf. [15, 28]), the projection of trial point $\mathbf{v} \in \left(L^2(\Omega)\right)^{p-1}$ onto $\mathcal{A}$ can be computed by the following algorithm:

Algorithm 3. Projection onto $\mathcal{A}$

Step 0. Initialization: given Ω, $\mathcal{A}_1$, $\mathcal{A}_2$, $\mathcal{A}_3$, $\mathbf{v}$, $\tau > 0$, k^{max}. Set $k \to 0$ and $\mathbf{w}^0 = \mathbf{v}$.

Step 1. Iterations: $\mathbf{w}^{k+1} = \mathscr{P}_{\mathcal{A}_3}\left[\mathscr{P}_{\mathcal{A}_2}\left[\mathscr{P}_{\mathcal{A}_1}[\mathbf{w}^k]\right]\right]$, Set $k \to k+1$.

Step 2. Stopping criteria: If $k = k^{max}$ or $\sum_{i=1}^{p-1} \|w_i^{k+1} - w_i^k\|_{L^2(\Omega)} \leqslant \tau$ stop the iterations and set $\mathscr{P}_{\mathcal{A}}[\mathbf{v}] \to \mathbf{w}^{k+1}$, else set $k \to k+1$ and goto step 1.

Proposition 3.3. *(Convergence theory of algorithms 3)Assuming $\mathcal{A} \neq \emptyset$, algorithms 3 is well defined and converges to the unique minimizer of* (49)

Proof. The proof is directly followed from the convergence theory of the classical alternating projections algorithm. It is well documented in the literature, see for instance [15, 28, 77]. □

4. Results and discussion

In this section we will evaluate the success and performance of algorithms 1 and 2 for the numerical solution of problems (5) and (35). For this purpose, it is assumed that Ω is a square with edge length equal to L, i.e., $\Omega = [0, L]^2$. The periodic boundary conditions is applied on $\partial\Omega$. Moreover, Ω is discretized into an $m \times m$ uniform grid with grid size $\Delta x = L/m$. The cell centered finite volume method is used for the spatial discretization of the continuum model, i.e. all quantities are defined at the centers of control volumes. The laplacian operator is discretized with the second order central-difference approach, i.e., $(\Delta u)^n_{i,j} = (u^n_{i,j+1} + u^n_{i+1,j} - 4u^n_{i,j} + u^n_{i-1,j} + u^n_{i,j-1})/\Delta x^2$ where $u^n_{i,j} := u^n(i\Delta x, j\Delta x)$. The complete MATLAB implementation of algorithms 1 and 2 and test cases studied in this section are given in the supplementary material of this paper. Therefore, to save the space, we avoid to discuss further details of the computational approach and refer interested readers to supplementary material. It is worth mentioning that the presented algorithms can be straightforwardly adapted when a pseudo spectral scheme (cf. [81]) like the fast fourier transform is used for the spatial discretization of laplacian and Helmholtz operators. For this purpose, it is sufficient to do the computations on the fourier space and whenever it is required to compute a nonlinear term and/or to apply a nonlinear operator (like the projection step), to switch to the real space and after performing the required procedure, to comeback to the fourier space.

The following symmetric double-well function, with wells located at $u = -1$ and $u = 1$ is considered in this section as the free energy density of the two-phase system with the uniform concentration field u,

$$F(u) = \frac{1}{4}\,(u^2 - 1)^2 \tag{50}$$

Similarly, the following p-well function is considered as the free energy density of the p-phase system with the uniform concentration field $\mathbf{u}$,

$$\mathbf{F}(\mathbf{u}) = \sum_{i=1}^{p} \frac{1}{4}\,(u_i^2 - 1)^2 \tag{51}$$

Considering functions (50) and (51), problems (5) and (35) will be nonconvex. Therefore, upon success, one expects that gradient descent algorithms 1 and 2 converge to a local minimum of the original optimization problems (50) and (51).

To evaluate practical success and performance of the presented algorithms, we will consider the solution of 26 test problems. The problems are defined such that in some cases the (approximate) overall distribution phases corresponding to the global minimizers are a-priori known. In all cases $\varepsilon = 1$, $L = 50$, $n = 50$, $\Delta t = 0.5$, $\delta = 0$, $\tau = \texttt{1.e-15}$, $\mu^{min} = \texttt{1.e-30}$, $\mu^{max} = \texttt{1.e+30}$, $k^{max} = \infty$, and the volume fraction of phases are assumed to be equal, i.e., $\Lambda_i = 2/p - 1$ for $i = 1, \ldots, p$ [1]. Considering the definition of $F(u)$ and $\mathbf{F}(\mathbf{u})$ respectively according to (50) and (51), the objective functional in our model problems approximately measures the total perimeter of inter-phase boundaries, c.f. [3, 58, 59][2], the global minimizers of our test problems are equivalent to the division of 2D space into equal partitions with least perimeters. To generate the initial distribution of phases in the spatial domain (generation of u_0 or $\mathbf{u}_0$), 5×5 squares of phases are randomly distributed in the discretized spatial domain such that the initial phases distribution satisfies the optimization constraints. Considering the original optimization problem in the present study is non-convex, the final solutions of algorithms 1 and 2 depend on the initial conditions. Therefore, the numerical result of every test problem can vary across multiple runs (consider the random generation of phases distribution). Except, in cases where explicitly stated, we run our code with the same initial conditions for a fixed value of p. However, to illustrate the impact of initial conditions on the final solutions, we will report our results for the same test cases that just differ in initial conditions.

[1] We fixed some parameters here to reduce the number of experiments. However, interested readers are encouraged to study the behaviors of algorithms numerically by changing other parameters, using the supplementary MATLAB codes.

[2] More precisely, the objective functional Γ-converges to the total perimeter of inter-phase boundaries as $\varepsilon \to 0$.

In the next subsection, we present numerical results of algorithm 1 and evaluate its practical behavior according to our results. Thereafter, in subsection 4.3, the behavior of algorithm 2 will be studied for three-phase systems throughout various numerical experiments. Finally, the algorithm 2 is evaluated numerically for the multiphase systems with more than three phases in the subsection 4.3.

4.1. **Numerical results of algorithm 1 (two phase problems).** Table 1 shows the details of parameters related to the test problems, test cases #1-#12, used in this work to study the behavior of algorithm 1. The column μ in this table refers to the method that is used to compute μ, i.e. `BB` denotes the computation of μ by the Barzilai-Borwein method and a number denotes the application of a constant value as μ. In test cases #1-#5, the same initial conditions are used and the parameter ϱ varies. In cases #6-#8, except the initial conditions, all parameters are similar to case #3, c.f. figure 1. In cases #9-#12, except μ all parameters and the initial conditions are identical to cases #3, #6, #7 and #8 respectively.

The evolution of solution with iterations for test cases #1-#5 is shown in figure 2. The final values of the objective functional corresponding to these cases are shown in table 2. According to these results, the final solution can be significantly changed by the variation of ϱ such that different branches of solution-space can possibly be explored by the variation of ϱ. Moreover, $\varrho = 1.0$ appears to be an optimal choice in these cases. It is worth to mention that the global minimizer of this problem is the separation of phases with the lamellar microstructure (cf. section 16.4 of [38]). Figure 3 shows the final solutions corresponding to test cases #3 and #6-#12. Figure 4 shows the variation of objective functional with iterations for test cases #3, #6, #9 and #10. The graphs are plotted in log-log scale to illustrate he details of variations near the final solutions. To avoid the singularity, the initial value of the objective functional (iteration equal to zero) is not included in the plots. According to the plots, as it is expected, algorithm 1 does not behave monotonically; however, it effectively reduces the objective functional after a sufficient number of iterations. Moreover, using $\mu = 1$ instead of computing μ by the Barzilai-Borwein approach leads to a more monotonic behavior of the algorithm (according to our numerical results, $\mu = 1$ is almost an optimal choice for this problem). Nevertheless, the optimal value of μ is problem dependent and it is not easy to determine μ a-priori. Considering table 2, the final value of the objective functional of the Barzilai-Borwein approach is almost equal to that of $\mu = 1$. Therefore, the application of the Barzilai-Borwein approach is recommended according to our numerical results.

TABLE 1. Parameters corresponding to test cases #1-#12 in the present study.

ID of Test Case	p	ϱ	μ	n^{max}	ID of Test Case	p	ϱ	μ	n^{max}
#1	2	0.25	BB	400	#7	2	1.0	BB	400
#2	2	0.5	BB	400	#8	2	1.0	BB	400
#3	2	1.0	BB	400	#9	2	1.0	1	400
#4	2	1.5	BB	400	#10	2	1.0	1	400
#5	2	2.0	BB	400	#11	2	1.0	1	400
#6	2	1.0	BB	400	#12	2	1.0	1	400

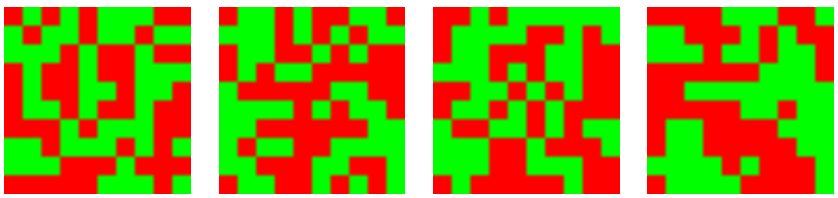

(a) #3 (b) #6 (c) #6 (d) #6

FIGURE 1. The initial conditions corresponding to test cases #3, #6, #7 and #8.

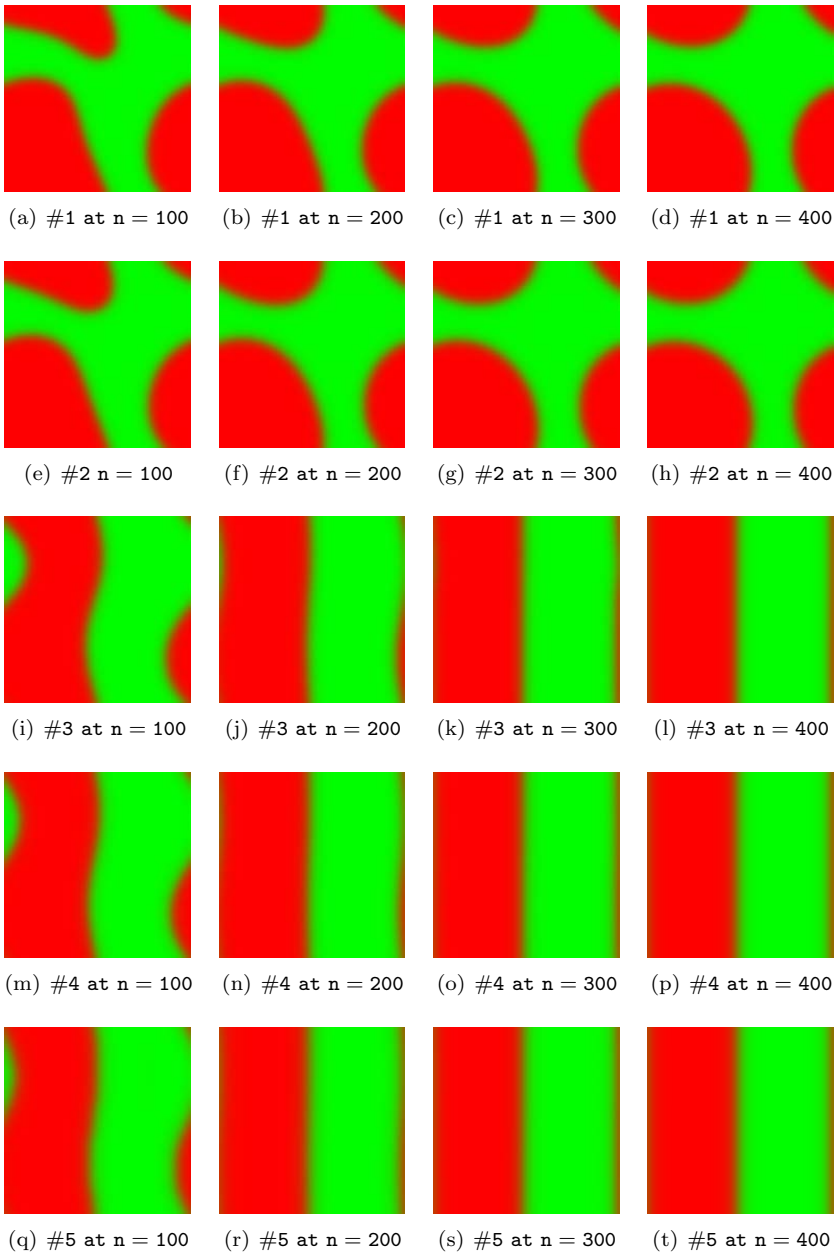

(a) #1 at n = 100 (b) #1 at n = 200 (c) #1 at n = 300 (d) #1 at n = 400

(e) #2 n = 100 (f) #2 at n = 200 (g) #2 at n = 300 (h) #2 at n = 400

(i) #3 at n = 100 (j) #3 at n = 200 (k) #3 at n = 300 (l) #3 at n = 400

(m) #4 at n = 100 (n) #4 at n = 200 (o) #4 at n = 300 (p) #4 at n = 400

(q) #5 at n = 100 (r) #5 at n = 200 (s) #5 at n = 300 (t) #5 at n = 400

FIGURE 2. The evolution of solution with iterations for test cases #1-#5.

TABLE 2. Final values of objective functional for test cases #1-#12 in the present study.

ID of Test Case	final value of E	ID of Test Case	final value of E
#1	138.9828	#7	134.7568
#2	138.3836	#8	157.7508
#3	109.6457	#9	109.3952
#4	111.6975	#10	140.0652
#5	111.6119	#11	134.6208
#6	140.1253	#12	157.5727

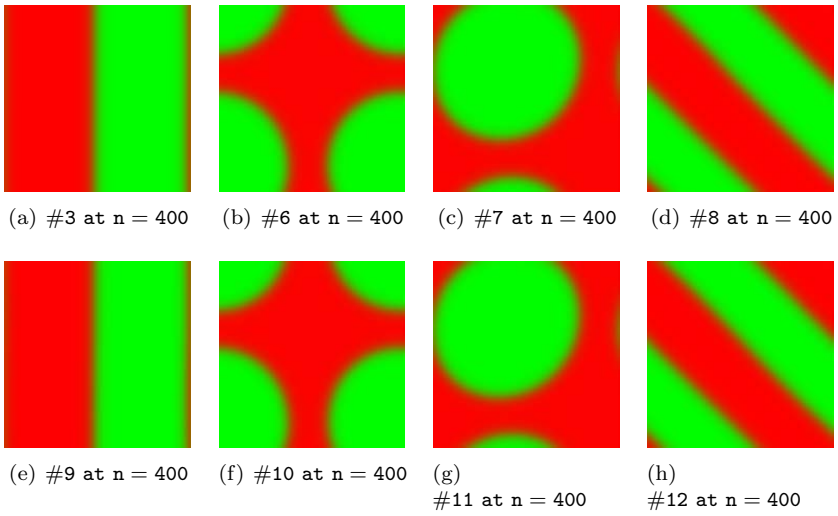

(a) #3 at n = 400 (b) #6 at n = 400 (c) #7 at n = 400 (d) #8 at n = 400

(e) #9 at n = 400 (f) #10 at n = 400 (g) #11 at n = 400 (h) #12 at n = 400

FIGURE 3. The final solutions of test cases #3 and #6-#12.

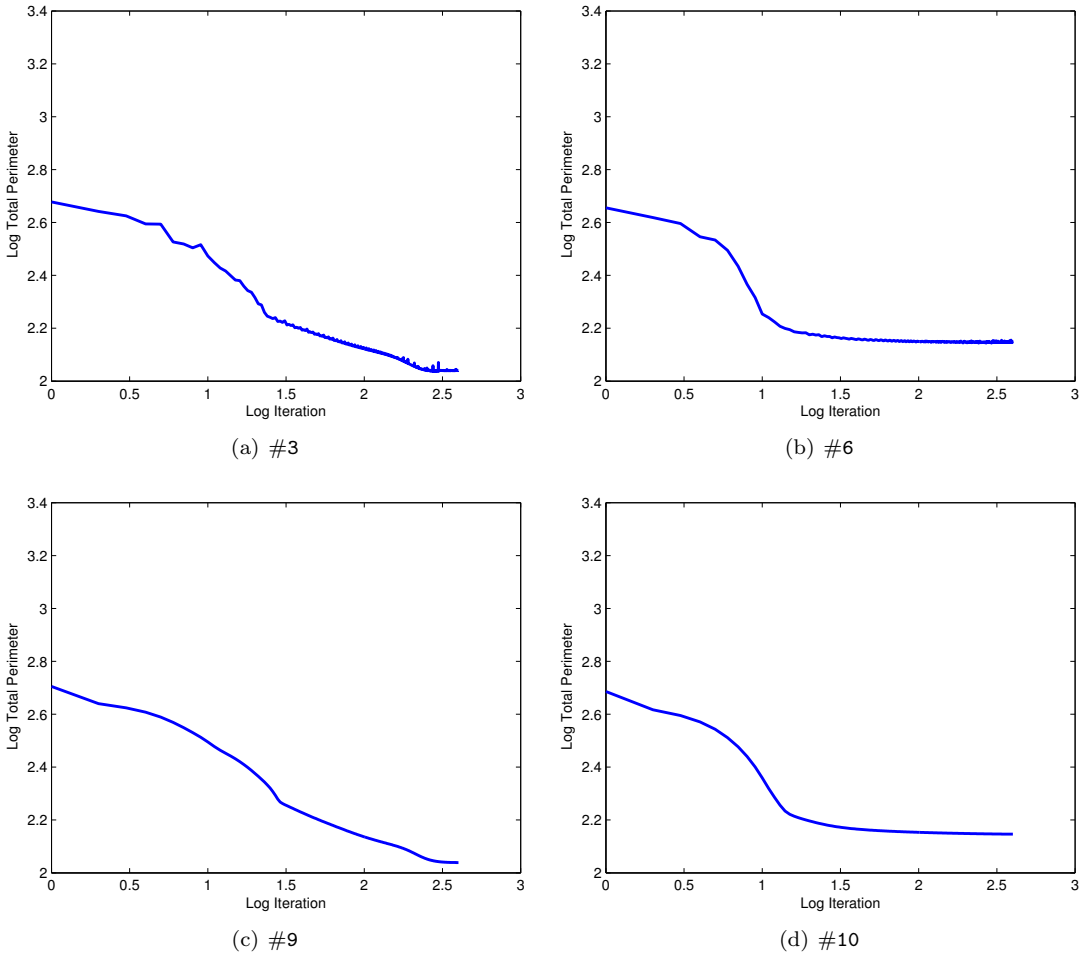

(a) #3 (b) #6

(c) #9 (d) #10

FIGURE 4. The objective functional vs. iteration for test cases #3, #6, #9 and #10.

To illustrate the effect of regularization procedure, step 1.3 of algorithm 1, on the behavior of algorithm 1, we run test case 3 without the regularization step, i.e. $\varrho = 0$. The final solution and the objective functional history of this experiment are shown in figure 5. Comparing these results to that of figure 4-a illustrates that the regularization step of algorithm 1 significantly improves the stability of algorithm 1. Comparing the final values of objective function, it is equal to `141.4675` in this experiment, demonstrates the numerical performance of using regularization step in practice. Furthermore, it appears that using the regularization step in algorithm 1 increases the chance of exploring the global minimizer of the original problem.

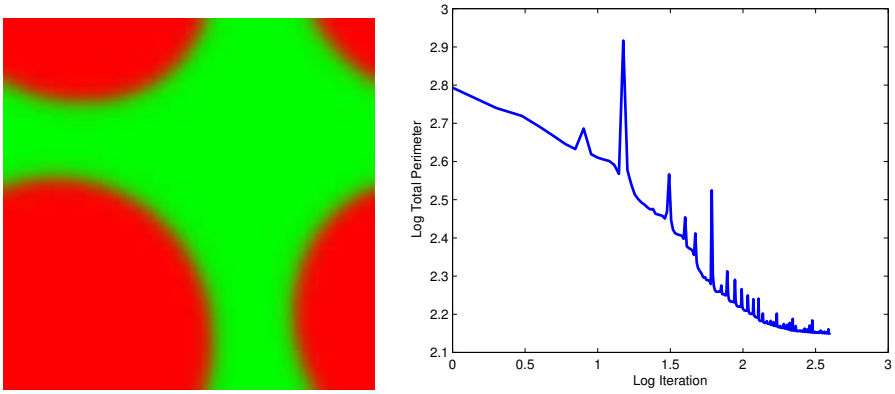

FIGURE 5. The results of running test case #3 without the regularization step ($\varrho = 0$): The final solution (left) and the objective functional history (right).

4.2. **Numerical results of algorithm 2 for three-phase problem.** According to our numerical experiments, by executing the code with different randomly generated initial conditions, there exist three topologically distinct morphologies as the stationary point of our three-phase model problem. They are called diagonally stretched honeycomb, lamellar, and mixed morphologies here. The initial conditions used in this subsection to generate these morphologies are shown in figure 6. To the best of our knowledge there is no analytical and/or numerical result on the structure of global minimizer of our three-phase model problem. Therefore, our quantitative results here possibly provides some insights about the morphology of the global minimizer. To evaluate the behavior of algorithm 2 in the case of three-phase problems, 10 test problems, called test cases #13-#22, are considered here. Table 3 shows details of parameters related to test cases #13-#22. Except test cases #21 and #22, the initial condition corresponding to the diagonally stretched honeycomb structure is used as the initial condition in all of the numerical experiments in this section.

The evolution of solution with the iterations are shown in figure 7-8 for test cases #13-#22. The corresponding final values of the objective functional are shown in table 4. Figure 9 shows the variation of objective functional with iterations for test cases #15, #18, #19 and #20.

According to our numerical results in this subsection, the presented algorithm, while behaves nonmonotonically, effectively reduces the objective functional and is successful in approaching to the optimal solution. Comparing the final values of the objective functional corresponding to test cases #15 and #18 demonstrates the computational performance of computing parameter μ with the Barzilai-Borwein approach. The same comparison between results of test cases #15, #19 and #20 illustrates the impact of the regularization step on the computational performance and the stability of algorithm 2. Furthermore, it can be conjectured that the mixed microstructure (c.f. figure 8 part (t)) is the global minimizer of the three-phase optimization problem considered in this subsection. This morphology includes the horizontal layers of phase 1 that is separated by vertical layers of phases 2 and 3, c.f. figure 10.

TABLE 3. Parameters corresponding to test cases #13-#22 in the present study.

ID of Test Case	p	ϱ	μ	n^{max}	ID of Test Case	p	ϱ	μ	n^{max}
#13	3	0.25	BB	600	#18	3	1.0	1	600
#14	3	0.5	BB	600	#19	3	0.0	BB	600
#15	3	1.0	BB	600	#20	3	0.0	1	600
#16	3	1.5	BB	600	#21	2	1.0	BB	600
#17	3	2.0	BB	600	#22	2	1.0	BB	600

TABLE 4. Final values of objective functional for test cases #13-#22 in the present study.

ID of Test Case	final value of $\mathbf{E}$	ID of Test Case	final value of $\mathbf{E}$
#13	364.2513	#14	365.2136
#15	365.2654	#16	365.8793
#17	376.3762	#18	370.0546
#19	379.0403	#20	3191.1534 (unstable)
#21	390.9506	#22	332.2796

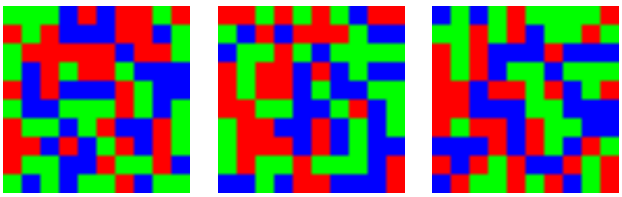

(a) (b) (c)

FIGURE 6. The initial conditions corresponding to three phase model problem in the present study, they results in diagonally stretched honeycomb (a), lamellar (b) and mixed (c) morphologies at the stationary points.

4.3. **Numerical results of algorithm 2 for more than three phases.** The computational outcome of algorithm 2 for the model problem introduced in section 4 is presented in this subsection for $p = 4$, 5 and 6. It is well known that when $p = 4$, the global minimizer is the periodic tessellation of Ω with a regular honeycomb structure. Because it is not possible to cut a square sub-domain that exactly includes 5 or 6 hexagons from an infinite regular honeycomb structure, it is not easy to determine the global solution when $p = 5$ and 6. However, as our numerical results in this section suggest, the periodic tessellation of domain with hexagonal-shaped sub-domains appears to be the global solution of cases $p = 5$ and 6. Table 5 shows details of parameters related to test cases used in this subsection. For $p = 4$, we run our code with two different randomly generated initial conditions. In fact test cases #23 and #24 use the same set of parameters, but different initial conditions.

The evaluation of solution during the optimization cycles is shown in figures 11 and 12 for test cases #23-#26. According to the plots, the results of test cases #23 and #24 are almost identical to the expected global solution. The final values of objective functional for these cases are respectively equal to 394.6009 and 395.4643. The final morphologies of test cases #25 and #26 are similarly the partitioning of the domain with hexagonally-shaped sub-domains. Therefore, we conjecture that for $p \geqslant 4$, the global solution of our model problem is the periodic tessellation of domain with hexagonal sub-domains. It will be identical to the regular honeycomb tessellation in certain cases like $p = 4$ and 8 etc. The variation of objective functional with iterations is shown in figure 13 for test cases #23-#26. According to the plots, the objective functional decreases monotonically by iterations at early states of optimization, and exhibits non-monotonic behavior near the optimal solution. It appears that the non-monotone stabilization of the optimization algorithm and the continuation on parameter ϱ can improve the behavior of algorithm 1 and 2 in practice.

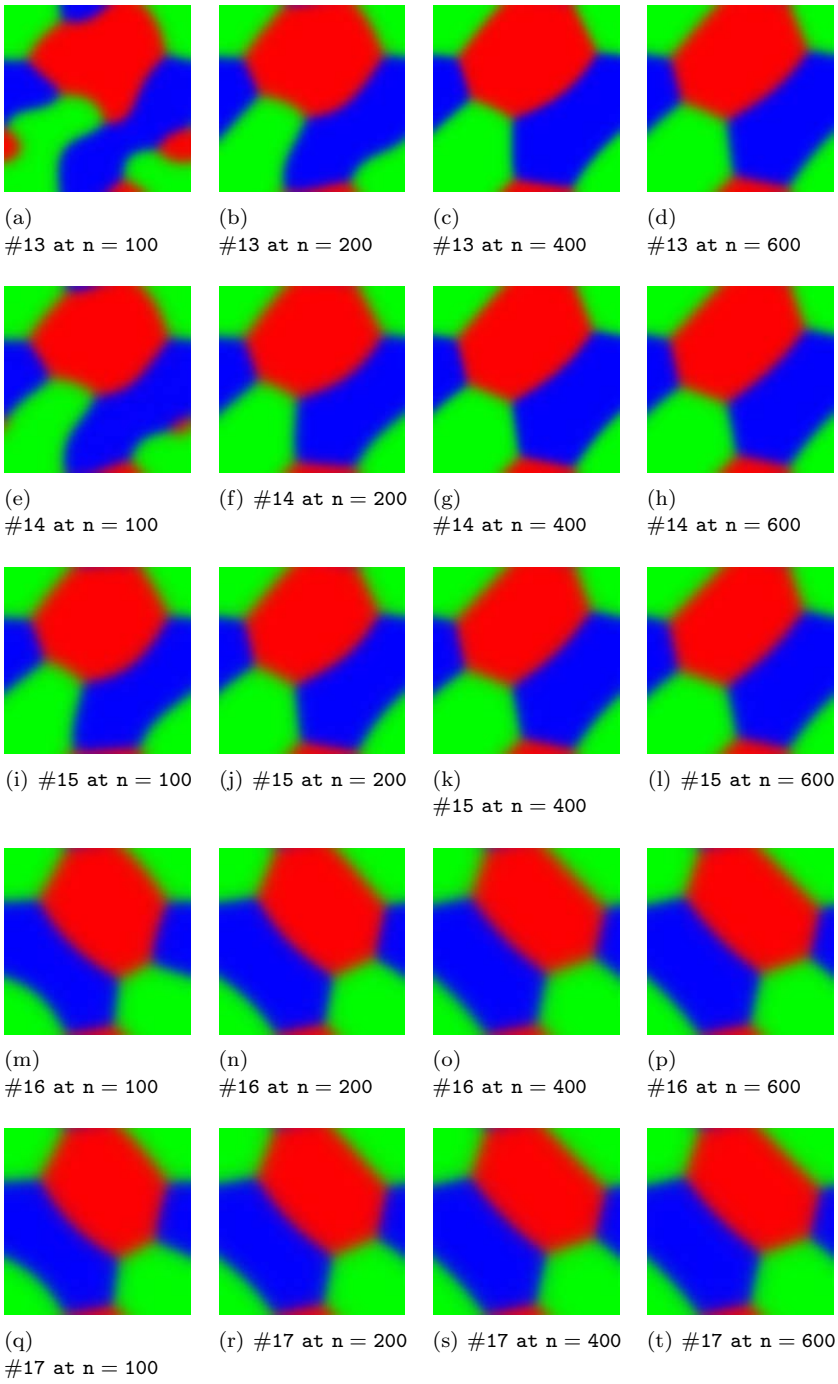

(a) #13 at n = 100
(b) #13 at n = 200
(c) #13 at n = 400
(d) #13 at n = 600
(e) #14 at n = 100
(f) #14 at n = 200
(g) #14 at n = 400
(h) #14 at n = 600
(i) #15 at n = 100
(j) #15 at n = 200
(k) #15 at n = 400
(l) #15 at n = 600
(m) #16 at n = 100
(n) #16 at n = 200
(o) #16 at n = 400
(p) #16 at n = 600
(q) #17 at n = 100
(r) #17 at n = 200
(s) #17 at n = 400
(t) #17 at n = 600

FIGURE 7. The evolution of solution with iterations for test cases #13-#17.

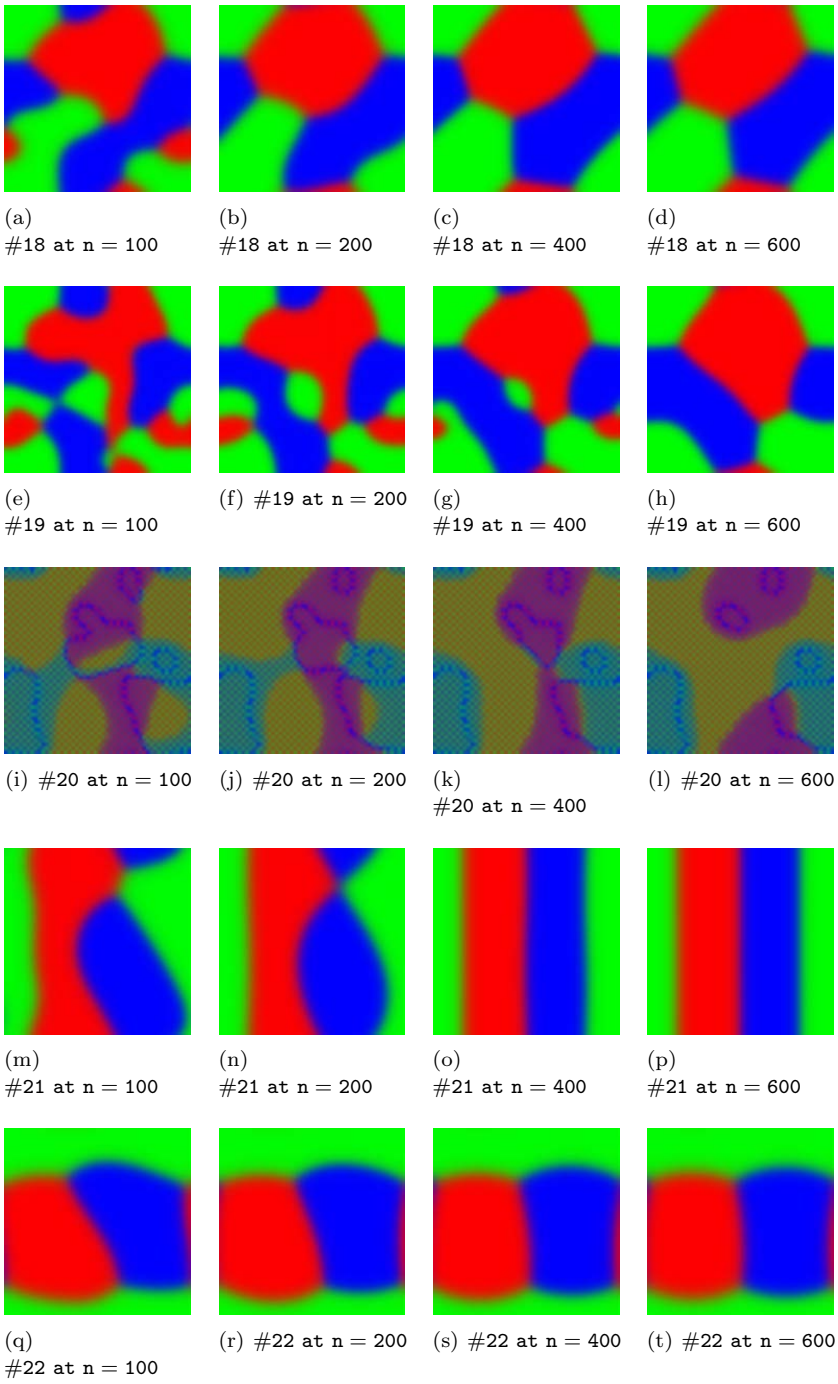

(a) #18 at n = 100 (b) #18 at n = 200 (c) #18 at n = 400 (d) #18 at n = 600

(e) #19 at n = 100 (f) #19 at n = 200 (g) #19 at n = 400 (h) #19 at n = 600

(i) #20 at n = 100 (j) #20 at n = 200 (k) #20 at n = 400 (l) #20 at n = 600

(m) #21 at n = 100 (n) #21 at n = 200 (o) #21 at n = 400 (p) #21 at n = 600

(q) #22 at n = 100 (r) #22 at n = 200 (s) #22 at n = 400 (t) #22 at n = 600

FIGURE 8. The evolution of solution with iterations for test cases #18-#22.

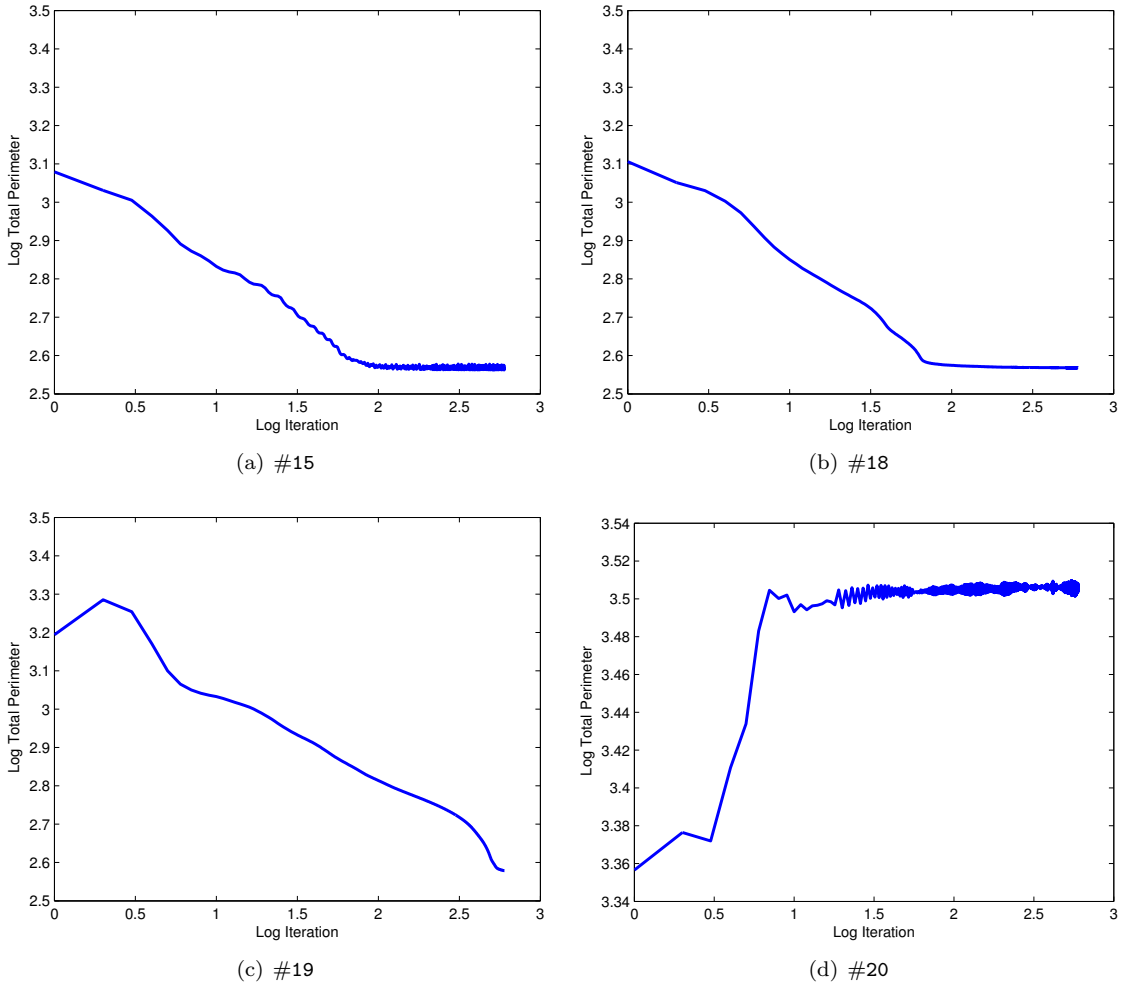

(a) #15 (b) #18

(c) #19 (d) #20

FIGURE 9. The objective functional vs. iteration for test cases #3, #6, #9 and #10.

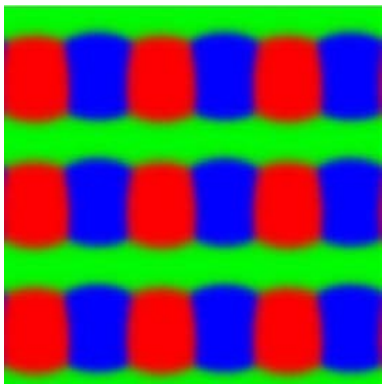

FIGURE 10. The conjectured global minimizer of three-phase model problem in the present study (the periodic tessellation of the 2D space by three equal partitions with least perimeters).

TABLE 5. Parameters corresponding to test cases #23-#26 in the present study.

ID of Test Case	p	ϱ	μ	n^{max}	ID of Test Case	p	ϱ	μ	n^{max}
#23	4	1.0	BB	1000	#25	5	1.0	BB	1000
#24	4	1.0	BB	1000	#26	6	1.0	BB	1000

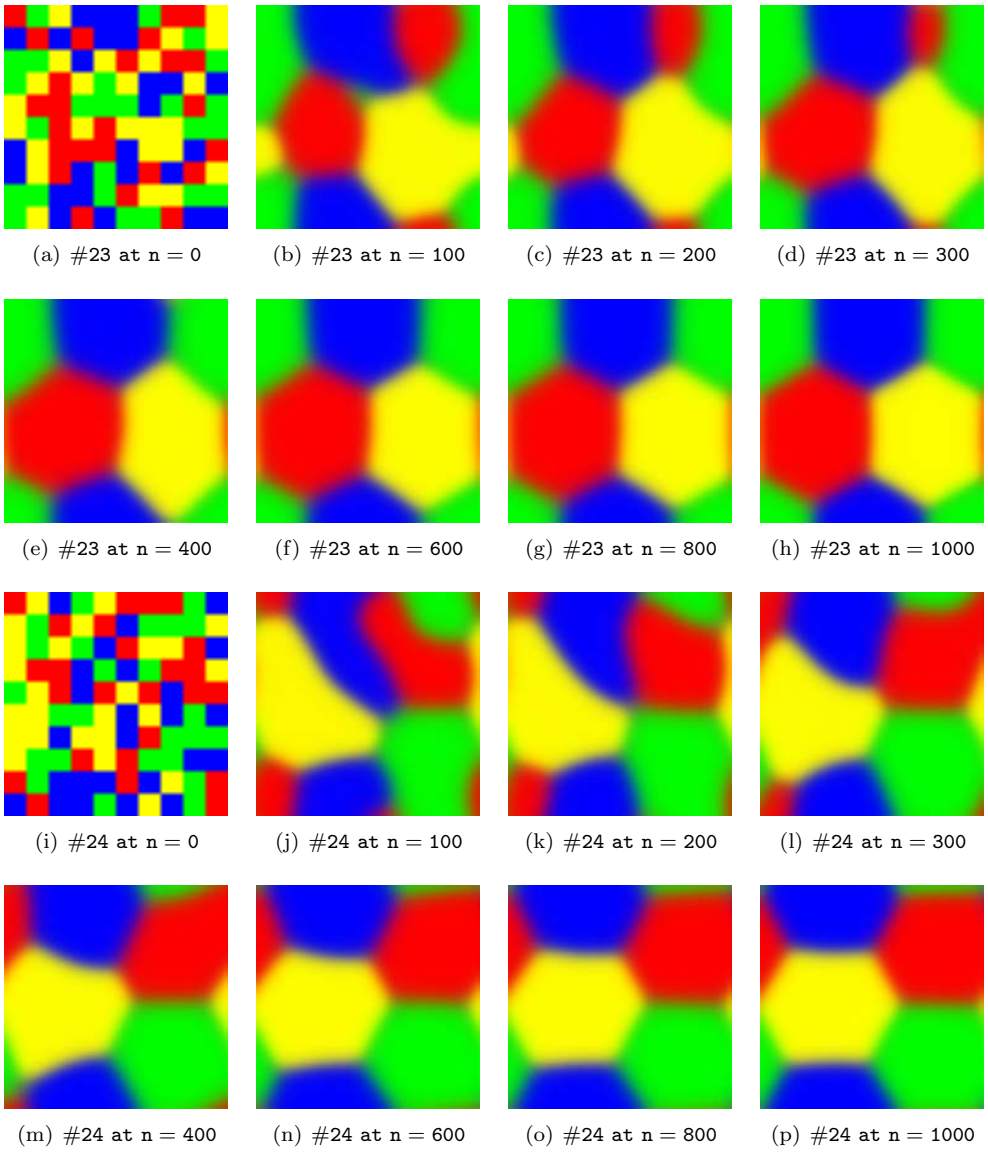

(a) #23 at n = 0 (b) #23 at n = 100 (c) #23 at n = 200 (d) #23 at n = 300

(e) #23 at n = 400 (f) #23 at n = 600 (g) #23 at n = 800 (h) #23 at n = 1000

(i) #24 at n = 0 (j) #24 at n = 100 (k) #24 at n = 200 (l) #24 at n = 300

(m) #24 at n = 400 (n) #24 at n = 600 (o) #24 at n = 800 (p) #24 at n = 1000

FIGURE 11. The evolution of solution with iterations for test cases #23 and #24.

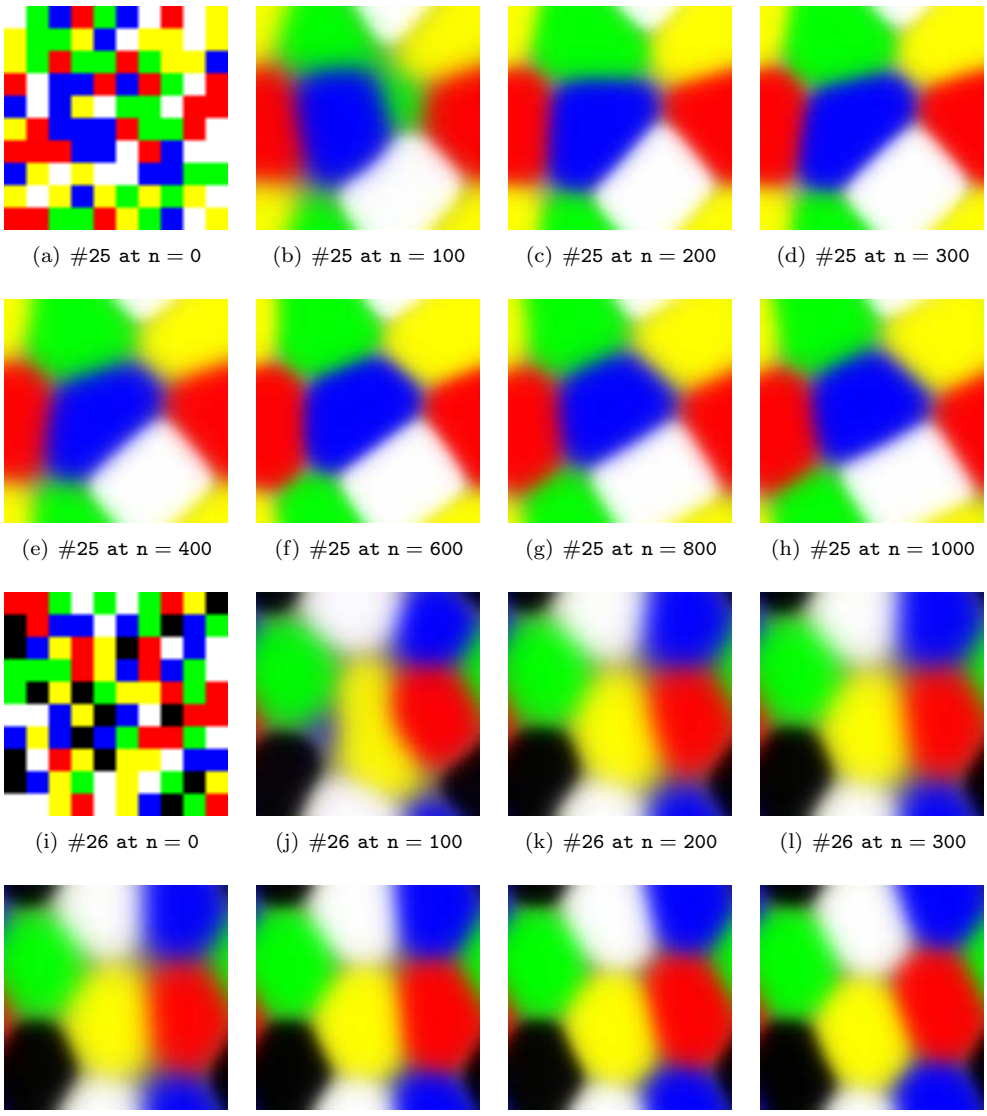

(a) #25 at n = 0 (b) #25 at n = 100 (c) #25 at n = 200 (d) #25 at n = 300

(e) #25 at n = 400 (f) #25 at n = 600 (g) #25 at n = 800 (h) #25 at n = 1000

(i) #26 at n = 0 (j) #26 at n = 100 (k) #26 at n = 200 (l) #26 at n = 300

(m) #26 at n = 400 (n) #26 at n = 600 (o) #26 at n = 800 (p) #26 at n = 1000

FIGURE 12. The evolution of solution with iterations for test cases #25 and #26.

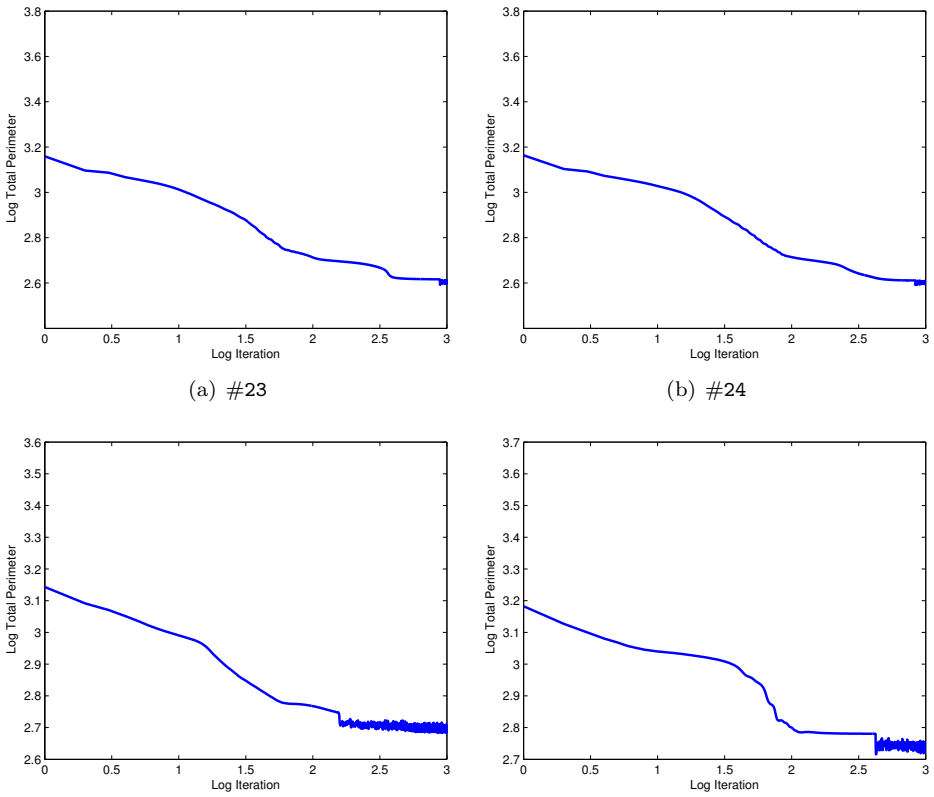

(a) #23 (b) #24

(c) #25 (d) #26

FIGURE 13. The objective functional vs. iteration for test cases #23-#26.

5. Conclusion

Two computational algorithms are developed in the present study to minimize the volume constrained Ginzburg-Landau Functional and its vector-valued version. These algorithms are based on the regularization of the objective functional with the Tikhonov regularization approach and performing the optimization iteratively using the regularized objective functional. Every iteration of the optimization procedure includes two steps. In the first step, the non-regularized volume constrained Ginzburg-Landau functional is minimized by the constrained steepest descent approach. To manage the set of constraints, the scaled projected gradient approach is included in the first step. The corresponding theory of this approach was discussed in details. The scaling factor of the projected gradient method is computed based on the Barzilai-Borwein approach that exhibits the spectral property without using second order derivative information. The second step of every optimization iteration regularizes the solution such that it enjoys the regularity of H^1 function space, while it respects to all corresponding constraints. The performance and success of the presented algorithms are studied throughout several numerical experiments. According to our numerical results, while no globalization strategy is used in the present work, the algorithms converged to approximate local minimums of the objective functionals to a good accuracy. Furthermore, numerical results clearly demonstrate the benefits of using the Barzilai-Borwein method and the developed regularization strategy. The presented algorithms can be easily extended to solve alternative problems with the similar set of constraints such as the conservative dynamics of vector-valued Swift-Hohenberg functional, called the multi-phase-field crystal equation. The nonmonotonic stabilization of the presented algorithms and the development of an appropriate continuation algorithm to dynamically change the regularization parameter are suggested as the scope of the future works.

References

[1] G. Allaire. *Numerical analysis and optimization: an introduction to mathematical modelling and numerical simulation*. Translated by: Craig, A., Oxford University Press, USA, 2007.

[2] S.M. Allen and J.W. Cahn. A microscopic theory for antiphase boundary motion and its application to antiphase domain coarsening. *Acta Metallurgica*, 27(6):1085–1095, 1979.

[3] S. Baldo. Minimal interface criterion for phase transitions in mixtures of cahn-hilliard fluids. *Ann Inst H. Poincaré (C) Anal Non Linéaire*, 7(2):67–90, 1990.

[4] R.W. Balluffi, S. Allen, and W. C. Carter. *Kinetics of materials*. John Wiley & Sons, 2005.

[5] J. Barzilai and J. Borwein. Two-point step size gradient methods. *IMA J Numer Anal*, 8(1):141–148, 1988.

[6] M. Beneš, S. Yazaki, and M. Kimura. Computational studies of non-local anisotropic allen-cahn equation. *Mathematica Bohemica*, 136(4):429–437, 2011.

[7] S. Bhattacharyya and T.A. Abinandanan. A study of phase separation in ternary alloys. *Bul Mater Sci*, 26(1):193–197, 2003.

[8] E. Birgin, J.M. Martınez, and M. Raydan. Spectral projected gradient methods: Review and perspectives. *J Statistical Software*, 60(3), 2014.

[9] E.G. Birgin, J.M. Martínez, and M. Raydan. Nonmonotone spectral projected gradient methods on convex sets. *SIAM J Optim*, 10(4):1196–1211, 2000.

[10] L. Blank, H. Garcke, L. Sarbu, and V. Styles. Primal-dual active set methods for allen–cahn variational inequalities with nonlocal constraints. *Numer Meth Part D E*, 29(3):999–1030, 2013.

[11] L. Blank, L. Sarbu, and M. Stoll. Preconditioning for allen–cahn variational inequalities with non-local constraints. *J Comput Phys*, 231(16):5406–5420, 2012.

[12] J. Bosch, M. Stoll, and P. Benner. Fast solution of cahn–hilliard variational inequalities using implicit time discretization and finite elements. *J Comput Phys*, 262:38–57, 2014.

[13] Jessica Bosch, David Kay, Martin Stoll, and Andrew J Wathen. Fast solvers for cahn–hilliard inpainting. *SIAM J Imaging Sci*, 7(1):67–97, 2014.

[14] P. Boyanova and M. Neytcheva. Efficient numerical solution of discrete multi-component cahn–hilliard systems. *Comput Math Appl*, 67(1):106–121, 2014.

[15] S. Boyd and J. Dattorro. Alternating projections. *Online note*, 2003. is available online at: `web.stanford.edu/class/ee392o/alt_proj.pdf`.

[16] S.P. Boyd and L. Vandenberghe. *Convex optimization*. Cambridge university press, 2004.

[17] M. Brassel and E. Bretin. A modified phase field approximation for mean curvature flow with conservation of the volume. *Math Method Appl Sci*, 34(10):1157–1180, 2011.

[18] J.W. Cahn. On spinodal decomposition. *Acta Metal*, 9(9):795–801, 1961.

[19] J.W. Cahn and J.E. Hilliard. Free energy of a nonuniform system. i. interfacial free energy. *J Chem Phys*, 28(2):258–267, 1958.

[20] J.W. Cahn and J.E. Hilliard. Free energy of a nonuniform system. iii. nucleation in a two-component incompressible fluid. *J Chem Phys*, 31(3):688–699, 1959.

[21] J.W. Cahn and J.E. Hilliard. Spinodal decomposition: A reprise. *Acta Metal*, 19(2):151–161, 1971.

[22] L. Chen. Computer simulation of spinodal decomposition in ternary systems. *Acta Metal Mater*, 42(10):3503–3513, 1994.

[23] J. Choi, H.G. Lee, D. Jeong, and J. Kim. An unconditionally gradient stable numerical method for solving the allen–cahn equation. *Physica A*, 388(9):1791–1803, 2009.

[24] M.I.M. Copetti. Numerical experiments of phase separation in ternary mixtures. *Math Comput Sim*, 52(1):41–51, 2000.

[25] S.M. Cox and P.C. Matthews. Exponential time differencing for stiff systems. *J Comput Phys*, 176(2):430–455, 2002.

[26] L. Cueto-Felgueroso and J. Peraire. A time-adaptive finite volume method for the cahn–hilliard and kuramoto–sivashinsky equations. *J Comput Phys*, 227(24):9985–10017, 2008.

[27] J.P. Desi, H.H. Edrees, J.J. Price, E. Sander, and T. Wanner. The dynamics of nucleation in stochastic cahn-morral systems. *SIAM J Appl Dyn Sys*, 10(2):707–743, 2011.

[28] R. Escalante and M. Raydan. *Alternating Projection Methods*, volume 8. SIAM, 2011.

[29] D.J. Eyre. Systems of cahn-hilliard equations. *SIAM J Appl Math*, 53(6):1686–1712, 1993.

[30] D.J. Eyre. Unconditionally gradient stable time marching the cahn-hilliard equation. In *MRS Proceedings*, volume 529, page 39. Cambridge Univ Press, 1998.

[31] D. Fan, C. Geng, and L. Chen. Computer simulation of topological evolution in 2-d grain growth using a continuum diffuse-interface field model. *Acta Mater*, 45(3):1115–1126, 1997.

[32] P.C. Fife. Models for phase separation and their mathematics. *Electron J Differ Equations*, 2000(48):1–26, 2000.
[33] R. Fletcher. On the Barzilai-Borwein method. *Applied Optimization, Vol. 96, Optimization and Control with Applications*, pages 235–256, 2001.
[34] H. Garcke, B. Nestler, B. Stinner, and F. Wendler. Allen–cahn systems with volume constraints. *Math Mod Meth Appl Sci*, 18(08):1347–1381, 2008.
[35] H. Garcke, B. Nestler, and B. Stoth. A multiphase field concept: numerical simulations of moving phase boundaries and multiple junctions. *SIAM J Appl Math*, 60(1):295–315, 1999.
[36] J.W. Gibbs. *On the equilibrium of heterogeneous substances*. Connecticut Academy Arts Sci, 1877.
[37] V.L. Ginzburg and L.D. Landau. On the theory of superconductivity. *Zh. Eksp. Teor. Fiz.*, 20(1064–1082), 1950 (english translation of this paper is available in L.D. Landau, Collected papers, Pergamon Press, Oxford, 1965).
[38] M.E. Glicksman. *Principles of solidification: an introduction to modern casting and crystal growth concepts*. Springer, 2010.
[39] H. Gómez, V.M. Calo, Y. Bazilevs, and T. Hughes. Isogeometric analysis of the cahn–hilliard phase-field model. *Comput Meth Appl Mech Eng*, 197(49):4333–4352, 2008.
[40] H. Gomez, A. Reali, and G. Sangalli. Accurate, efficient, and (iso) geometrically flexible collocation methods for phase-field models. *J Comput Phys*, 262:153–171, 2014.
[41] L. Grippo, F. Lampariello, and S. Lucidi. A nonmonotone line search technique for Newton's method. *SIAM Journal on Numerical Analysis*, pages 707–716, 1986.
[42] F. Guillén-González and G. Tierra. On linear schemes for a cahn–hilliard diffuse interface model. *J Comput Phys*, 234:140–171, 2013.
[43] U. Hecht, L. Gránásy, T. Pusztai, B. Böttger, M. Apel, V. Witusiewicz, L. Ratke, J. DeWilde, L. Froyen, and D. Camel. Multiphase solidification in multicomponent alloys. *Mater Sci Eng R*, 46(1):1–49, 2004.
[44] J.J. Hoyt. The continuum theory of nucleation in multicomponent systems. *Acta Metal Mater*, 38(8):1405–1412, 1990.
[45] J.J. Hoyt. Linear spinodal decomposition in a regular ternary alloy. *Acta Metal Mater*, 38(2):227–231, 1990.
[46] A.K. Kassam and L.N. Trefethen. Fourth-order time-stepping for stiff pdes. *SIAM J Sci Comput*, 26(4):1214–1233, 2005.
[47] D. Kay and R. Welford. A multigrid finite element solver for the cahn–hilliard equation. *J Comput Phys*, 212(1):288–304, 2006.
[48] J. Kim, K. Kang, and J. Lowengrub. Conservative multigrid methods for cahn–hilliard fluids. *J Comput Phys*, 193(2):511–543, 2004.
[49] J. Kim, S. Lee, and Y. Choi. A conservative allen–cahn equation with a space–time dependent lagrange multiplier. *Int J Eng Sci*, 84:11–17, 2014.
[50] J.S. Kirkaldy. A ginzburg-landau treatment of ternary spinodal decomposition. *J Mater Sci*, 35(5):1177–1180, 2000.
[51] R. Kornhuber and R. Krause. Robust multigrid methods for vector-valued allen–cahn equations with logarithmic free energy. *Comput Vis Sci*, 9(2):103–116, 2006.
[52] C.E. Krill I. and L. Chen. Computer simulation of 3-d grain growth using a phase-field model. *Acta Mater*, 50(12):3059–3075, 2002.
[53] A.G. Lamorgese, D. Molin, and R. Mauri. Phase field approach to multiphase flow modeling. *Milan J Math*, 79(2):597–642, 2011.
[54] H. Lee, J. Choi, and J. Kim. A practically unconditionally gradient stable scheme for the n-component cahn–hilliard system. *Physica A*, 391(4):1009–1019, 2012.
[55] H.G. Lee and J. Kim. An efficient and accurate numerical algorithm for the vector-valued allen–cahn equations. *Comput Phys Commun*, 183(10):2107–2115, 2012.
[56] Y. Li, H.G. Lee, D. Jeong, and J. Kim. An unconditionally stable hybrid numerical method for solving the allen–cahn equation. *Comput Math Appl*, 60(6):1591–1606, 2010.
[57] J. Liu, L. Dedè, J.A. Evans, M.J. Borden, and T. Hughes. Isogeometric analysis of the advective cahn–hilliard equation: spinodal decomposition under shear flow. *J Comput Phys*, 242:321–350, 2013.
[58] L. Modica. The gradient theory of phase transitions and the minimal interface criterion. *Arch Rat Mech Anal*, 98(2):123–142, 1987.
[59] L. Modica and S. Mortola. Un esempio di γ-convergenza. *Boll. Un. Mat. Ital. B*, 14(1):285–299, 1977.
[60] J.E. Morral and J.W. Cahn. Spinodal decomposition in ternary systems. *Acta Metal*, 19(10):1037–1045, 1971.

[61] Y. Nesterov and A. Nemirovskii. *Interior-point polynomial algorithms in convex programming*, volume 13. SIAM, 1994.
[62] B. Nestler and A. Choudhury. Phase-field modeling of multi-component systems. *Current Opinion Solid State Mater Sci*, 15(3):93–105, 2011.
[63] B. Nestler, F. Wendler, M. Selzer, B. Stinner, and H. Garcke. Phase-field model for multiphase systems with preserved volume fractions. *Phys Rev E*, 78(1):011604, 2008.
[64] J.W. Neuberger. Sobolev gradients and differential equations. *Lecture Notes in Mathematics*, 1670, 2010.
[65] J. Nocedal and S. Wright. *Numerical optimization*. Springer, 2006.
[66] N. Provatas and K. Elder. *Phase-field methods in materials science and engineering*. John Wiley & Sons, 2010.
[67] N. Raza, S. Sial, and A.R. Butt. Numerical approximation of time evolution related to ginzburg–landau functionals using weighted sobolev gradients. *Comput Math Appl*, 67(1):210–216, 2014.
[68] N. Raza, S. Sial, and S. Siddiqi. Approximating time evolution related to ginzburg–landau functionals via sobolev gradient methods in a finite-element setting. *J Comput Phys*, 229(5):1621–1625, 2010.
[69] N. Raza, S. Sial, and S.S. Siddiqi. Sobolev gradient approach for the time evolution related to energy minimization of ginzburg–landau functionals. *J Comput Phys*, 228(7):2566–2571, 2009.
[70] J.S. Rowlinson. Translation of jd van der waals'the thermodynamik theory of capillarity under the hypothesis of a continuous variation of density. *J Stat Phys*, 20(2):197–200, 1979.
[71] J. Rubinstein and P. Sternberg. Nonlocal reactiondiffusion equations and nucleation. *IMA J of Appl Math*, 48(3):249–264, 1992.
[72] J. Shen and X. Yang. Numerical approximations of allen-cahn and cahn-hilliard equations. *DISCRETE CONT DYN S A*, 28:1669–1691, 2010.
[73] S. Sial, J. Neuberger, T. Lookman, and A. Saxena. Energy minimization using sobolev gradients: application to phase separation and ordering. *J Comput Phys*, 189(1):88–97, 2003.
[74] Irina Singer-Loginova and HM Singer. The phase field technique for modeling multiphase materials. *Reports Progress Phys*, 71(10):106501, 2008.
[75] I. Steinbach, F. Pezzolla, B. Nestler, M. Seeßelberg, R. Prieler, G.J. Schmitz, and J. Rezende. A phase field concept for multiphase systems. *Physica D*, 94(3):135–147, 1996.
[76] B. Stinner, B. Nestler, and H. Garcke. A diffuse interface model for alloys with multiple components and phases. *SIAM J Appl Math*, 64(3):775–799, 2004.
[77] R. Tavakoli. On the coupled continuous knapsack problems: projection onto the volume constrained gibbs n-simplex. *Optimization Letters (in press)*, 2015.
[78] R. Tavakoli and H. Zhang. A nonmonotone spectral projected gradient method for large-scale topology optimization problems. *Numer Algebra, Control Optim*, 2(2):395–412, 2012.
[79] Rouhollah Tavakoli. Multimaterial topology optimization by volume constrained allen–cahn system and regularized projected steepest descent method. *Comput Meth Appl Mech Eng*, 276:534–565, 2014.
[80] Rouhollah Tavakoli and Seyyed Mohammad Mohseni. Alternating active-phase algorithm for multimaterial topology optimization problems: a 115-line matlab implementation. *Struct Multidisc Optim*, 49(4):621–642, 2014.
[81] Lloyd N Trefethen. *Spectral methods in MATLAB*, volume 10. SIAM, 2000.
[82] L. Vanherpe, F. Wendler, B. Nestler, and S. Vandewalle. A multigrid solver for phase field simulation of microstructure evolution. *Math Comput Sim*, 80(7):1438–1448, 2010.
[83] B.P. Vollmayr-Lee and A.D. Rutenberg. Fast and accurate coarsening simulation with an unconditionally stable time step. *Phys Rev E*, 68(6):066703, 2003.
[84] S. Wise, J. Kim, and J. Lowengrub. Solving the regularized, strongly anisotropic cahn–hilliard equation by an adaptive nonlinear multigrid method. *J Comput Phys*, 226(1):414–446, 2007.
[85] O. Wodo and B. Ganapathysubramanian. Computationally efficient solution to the cahn–hilliard equation: Adaptive implicit time schemes, mesh sensitivity analysis and the 3d isoperimetric problem. *J Comput Phys*, 230(15):6037–6060, 2011.
[86] S.J. Wright. *Primal-dual interior-point methods*, volume 54. SIAM, 1997.
[87] L. Zhang, M.R. Tonks, D. Gaston, J.W. Peterson, D. Andrs, P.C. Millett, and B.S. Biner. A quantitative comparison between c0 and c1 elements for solving the cahn–hilliard equation. *J Comput Phys*, 236:74–80, 2013.
[88] Z. Zhang and Z. Qiao. An adaptive time-stepping strategy for the cahn-hilliard equation. *Commun Comput Phys*, 11:1261–1278, 2012.